Article

Current Biology

The Diverged Trypanosome MICOS Complex as a Hub for Mitochondrial Cristae Shaping and Protein Import

Graphical Abstract

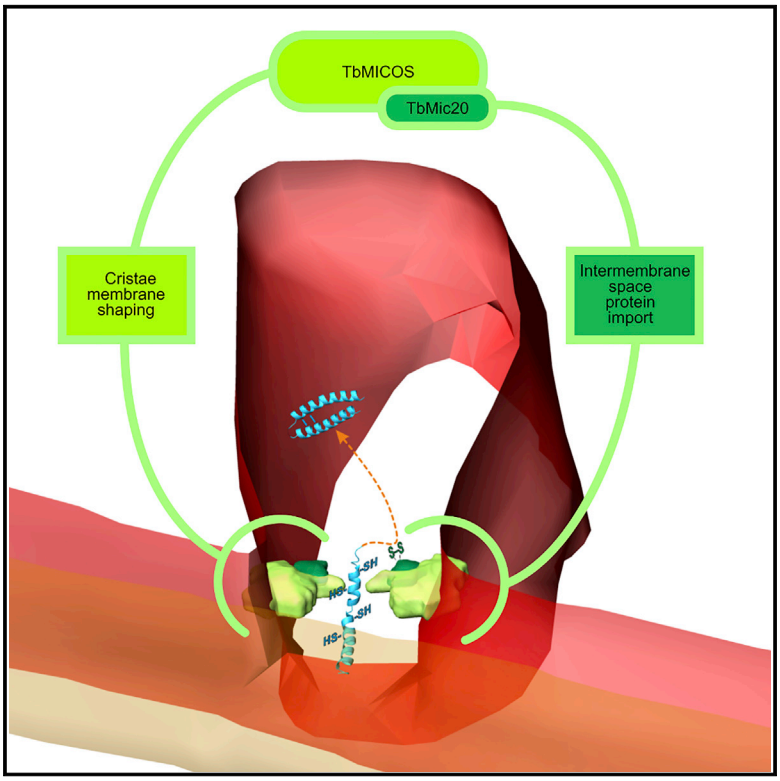

Authors

Iosif Kaurov, Marie Vancová, Bernd Schimanski, ..., André Schneider, Julius Lukeš, Hassan Hashimi

Correspondence

hassan@paru.cas.cz

In Brief

The mitochondrial contact site and cristae organizing system (MICOS) is a conserved feature of mitochondria. Kaurov et al. identify and characterize MICOS proteins outside of opisthokonts in the kinetoplastid parasite *Trypanosoma brucei*. TbMICOS plays a conserved role in mitochondrial cristae shaping and harbors several unique features as well.

Highlights

- First study of MICOS outside opisthokonts verifies a conserved role in shaping cristae
- Trypanosome MICOS novelties include two distinct Mic10s and an atypical Mic60
- TbMICOS features a novel thioredoxin-like subunit called TbMic20
- TbMic20 appears to be a catalyst for intermembrane space protein import

Kaurov et al., 2018, Current Biology *28*, 1–15
November 5, 2018
https://doi.org/10.1016/j.cub.2018.09.008

CellPress

Please cite this article in press as: Kaurov et al., The Diverged Trypanosome MICOS Complex as a Hub for Mitochondrial Cristae Shaping and Protein Import, Current Biology (2018), https://doi.org/10.1016/j.cub.2018.09.008

Current Biology
Article

The Diverged Trypanosome MICOS Complex as a Hub for Mitochondrial Cristae Shaping and Protein Import

Iosif Kaurov,[1,2] Marie Vancová,[1,2] Bernd Schimanski,[3] Lawrence Rudy Cadena,[2] Jiří Heller,[1] Tomáš Bílý,[1,2] David Potěšil,[4] Claudia Eichenberger,[3] Hannah Bruce,[2,7] Silke Oeljeklaus,[5] Bettina Warscheid,[5,6] Zbyněk Zdráhal,[4] André Schneider,[3] Julius Lukeš,[1,2] and Hassan Hashimi[1,2,8,*]

[1]Institute of Parasitology, Biology Center, Czech Academy of Sciences, 37005 České Budějovice, Czech Republic
[2]Faculty of Science, University of South Bohemia, 37005 České Budějovice, Czech Republic
[3]Department of Chemistry and Biochemistry, University of Bern, 3012 Bern, Switzerland
[4]Central European Institute of Technology, Masaryk University, 62500 Brno, Czech Republic
[5]Faculty of Biology, Biochemistry and Functional Proteomics, Institute of Biology II, University of Freiburg, 79104 Freiburg, Germany
[6]BIOSS Centre for Biological Signaling Studies, University of Freiburg, 79104 Freiburg, Germany
[7]Present address: Genome Research, Ltd., Wellcome Sanger Institute, Wellcome Genome Campus, Hinxton, Cambridge, UK
[8]Lead Contact
*Correspondence: hassan@paru.cas.cz
https://doi.org/10.1016/j.cub.2018.09.008

SUMMARY

The mitochondrial contact site and cristae organization system (MICOS) is a multiprotein complex responsible for cristae formation. Even though cristae are found in all mitochondria capable of oxidative phosphorylation, only Mic10 and Mic60 appear to be conserved throughout eukaryotes. The remaining 4 or 5 known MICOS subunits are specific to the supergroup Opisthokonta, which includes yeast and mammals that are the only organisms in which this complex has been analyzed experimentally. We have isolated the MICOS from *Trypanosoma brucei*, a member of the supergroup Excavata that is profoundly diverged from opisthokonts. We show that it is required for the maintenance of the unique discoidal cristae that typify excavates, such as euglenids and kinetoplastids, the latter of which include trypanosomes. The trypanosome MICOS consists of 9 subunits, most of which are essential for normal growth. Unlike in opisthokonts, it contains two distinct Mic10 orthologs and an unconventional putative Mic60 that lacks a mitofilin domain. Interestingly, one of the essential trypanosomatid-specific MICOS subunits called TbMic20 is a thioredoxin-like protein that appears to be involved in import of intermembrane space proteins, including respiratory chain complex assembly factors. This result points to trypanosome MICOS coordinating cristae shaping and population of its membrane with proteins involved in respiration, the latter via the catalytic activity of TbMic20. Thus, trypanosome MICOS allows us to define which of its features are conserved in all eukaryotes and decipher those that represent lineage-specific adaptations.

INTRODUCTION

Cristae are mitochondrial inner membrane (MIM) invaginations that are the organelle's morphological hallmark. They are distributed throughout eukaryotes, inherited from the last eukaryotic common ancestor (LECA) [1, 2]. Cristae assume different forms, with lamellar ones found in the best-studied supergroup Opisthokonta, which encompasses yeast and animals. Tubular-shaped cristae typify the unicellular supergroup SAR, containing stramenopiles, alveolates, and rhizarians. Euglenid members of the protistan supergroup Excavata generally have discoidal cristae, which exhibit a paddle-like morphology. Thus, cristae have evolved different morphologies that may represent adaptions to the multifarious cellular milieus of diverse eukaryotes.

Cristae occurrence correlates with an aerobic lifestyle mediated by mitochondria. This is because cristae membranes are enriched with respiratory chain complexes that perform oxidative phosphorylation (OXPHOS) [3–5]. Such a configuration boosts OXPHOS capacity by increasing the surface area for this process and concentrating the soluble electron carrier cytochrome *c* in the lumen enclosed by the cristae membrane [6, 7].

Pioneering studies in yeast identified a key multiprotein complex for cristae biogenesis called the mitochondrial contact site and cristae organizing system (MICOS) [8–10]. In this and other opisthokonts, the MICOS complex has been shown to maintain cristae junctions (CJs), narrow necks attaching cristae to the MIM [11–13]. The evolutionarily conserved core subunits Mic10 and Mic60 catalyze formation of negative curvature at CJs [14–16]. MICOS also forms contacts with mitochondrial outer membrane (MOM) proteins via Mic60's conserved C-terminal mitofilin domain. This domain is an intermembrane space (IMS) extension that interacts with the β-barrel protein sorting and assembly machinery subunit Sam50 and the protein translocase of the outer membrane (TOM) [17–19]. Furthermore, the mitofilin domain has been reported to augment the mitochondrial IMS import and assembly (MIA) pathway in yeast by interaction with the central MIA catalyst Mia40 [10].

By an oxidative folding mechanism, MIA sequesters small cysteine-rich proteins bearing twin CX_3C or CX_9C motifs [20, 21]. Mia40 catalyzes this folding through its reactive CPC motif, forming an intermolecular disulfide bond with a thiol group of a reduced and unfolded IMS precursor [22]. With Erv1, an IMS sulfhydryl oxidase, two intramolecular disulfide bridges linking each of the dual $CX_{3,9}C$ motifs are formed, creating a hairpin fold that traps substrate proteins within the IMS. During this process, Erv1 reoxidizes Mia40 for another round of translocation.

The mechanistic model of MICOS function has been proposed based on data gained solely from opisthokonts [11–13]. However, the majority of identified MICOS subunits are restricted to this clade. Only the Mic10 and Mic60 core subunits have a wide distribution overlapping with the occurrence of cristae [1, 2]. This strongly indicates that the ancestor of MICOS was already present in LECA. Mic60 may even pre-date MICOS, supported by evidence that it originates from the proteobacterial endosymbiont giving rise to mitochondria [1, 2]. Hitherto unidentified supernumerary MICOS subunits interacting with the ancient core may contribute to the diverse cristae morphologies of eukaryotes.

Thus, true insight into how the ancient and ubiquitous MICOS shapes cristae in eukaryotes requires mechanistic studies outside of the single opisthokont clade. The discipline of evolutionary cell biology postulates that a comparative approach to examining a biological system in different organisms can reveal chemical and physical constraints to their evolution [23]. Conversely, this approach can also identify a system's more flexible attributes, from which novelties may potentially emerge in certain lineages. The *in silico* approach to address the evolutionary cell biology of MICOS has reached saturation, necessitating functional data from other eukaryotic groups.

To this end, we have undertaken the first study of MICOS composition and function outside of opisthokonts. We have chosen the pathogen *Trypanosoma brucei* as our model, not only for its robust genetic toolkit but also because of its suitability for tackling the evolutionary cell biology of MICOS. *T. brucei* is a kinetoplastid belonging to the supergroup Excavata and therefore has an extended independent evolutionary history [24]. Its single mitochondrion undergoes massive remodeling during its life cycle [25]. The procyclic stage (PS) infecting the tsetse fly midgut has a mitochondrion with extensive discoidal cristae and OXPHOS capacity and thus is the focus here. The long slender bloodstream stage (BS) infecting mammalian hosts lacks both cristae and OXPHOS. Furthermore, *Mic10* was the only MICOS ortholog found in *T. brucei* by bioinformatics methods alone [1, 2], hinting at the tantalizing possibility of its MICOS bearing novel properties.

RESULTS

Trypanosomatids Have Two Mic10 Paralogs

Trypanosomatid Mic10 is made up of two well-supported clades [1] (Figure 1A). In *T. brucei*, these paralogs are represented by TbMic10-1 and TbMic10-2 (TbMic10-1/2) (Figure 1B). Mic10 duplication does not pre-date the emergence of trypanosomatids, because there is only one Mic10 ortholog found in the *Euglena gracilis* [26] and *Bodo saltans* genomes [27], representing their free-living sister groups. Although *B. saltans* Mic10 clearly belongs to the TbMic10-1 clade, the *E. gracilis* homolog cannot be assigned to either with high confidence.

As Mic10 family members, each *T. brucei* paralog contains two transmembrane domains (TMDs) (Figure 1B). The C-proximal TMD2 has a highly conserved GxGxGxG motif, which mediates Mic10 oligomerization required for membrane bending in yeast [14, 16]. The motif is conserved in the TbMic10-1 clade, whereas it is abbreviated to 3 alternating Gs in the TbMic10-2 clade (Figures 1B and S1A).

Both paralogs share some features that distinguish them from the best-characterized *Saccharomyces cerevisiae* Mic10 (Figure S1A). The TMD1 glycine-rich motif essential for Mic10 oligomerization is dramatically reduced in TbMic10-1/2. Furthermore, the *T. brucei* paralogs lack the positively charged KRR loop between the TMDs needed for MIM targeting of the yeast homolog [16]. Surprisingly, the KKR loop is absent in Mic10 orthologs of all eukaryotes outside the opisthokonts (Figure S1A). This fact underscores the need to study MICOS in other organisms like *T. brucei*.

TbMic10 Paralogs Shape Cristae

C-terminal V5-epitope-tagged TbMic10 paralogs show a patchy mitochondrial localization by indirect immunofluorescence (Figure 1C). To further investigate whether TbMic10-1/2 associate with cristae, immunogold labeling of the V5 epitopes on Tokuyasu cryosections were viewed by transmission electron microscopy (TEM) or electron tomography (ET). Nanoparticles (NPs) immunodecorating TbMic10-1-V5 and TbMic10-2-V5 were mainly observed at cristae membranes (Figure 1D; Video S1).

Next, we addressed whether TbMic10-1/2 are involved in shaping cristae. Initial attempts to delete either *TbMic10-1* or *TbMic10-2* by gene knockout did not yield any obvious phenotype, suggesting their functional redundancy. Thus, we generated cells in which both paralogs were ablated simultaneously by tetracycline-inducible RNAi silencing of TbMic10-2 in a TbMic10-1 deletion background (Figure S2). Cryosections derived from *ΔTbMic10-1*:TbMic10-2↓ 1 and 4 days post-induction (dpi) of RNAi were examined by TEM. At 4 dpi, cristae were significantly elongated compared to the parental cell line, sometimes as stacked semi-circles or arcs (Figure 2A). The severity of this phenotype correlates with time of induction, as it is less pronounced yet present at 1 dpi (Figure 6C).

Stacking of elongated cristae was also observed in yeast Mic10 deletion mutants in conjunction with CJ loss [8–10]. Because the slender CJs of discoidal cristae are difficult to observe on ultrathin cryosections, a 3D reconstruction of serial TEM cryosections was performed on *ΔTbMic10-1*:TbMic10-2↓ 4 dpi, which allows better assessment of CJ loss thanks to a broad z axis (Figures 2B and 2C; Video S2). The aberrant cristae were barrel shaped with finger-like projections extending from one end. CJs were not observed along the examined ~700 nm. In conclusion, the TbMic10 paralogs function synergistically in shaping of cristae and CJ biogenesis in PS *T. brucei*, thus confirming its hypothetical role outside of opisthokonts.

TbMic10 Paralogs Are Part of a Multi-protein Complex

Blue native PAGE of digitonin-solubilized mitochondrial membranes resolved a >1-MDa complex containing TbMic10-1, likely corresponding to *T. brucei* MICOS, with potential intermediates

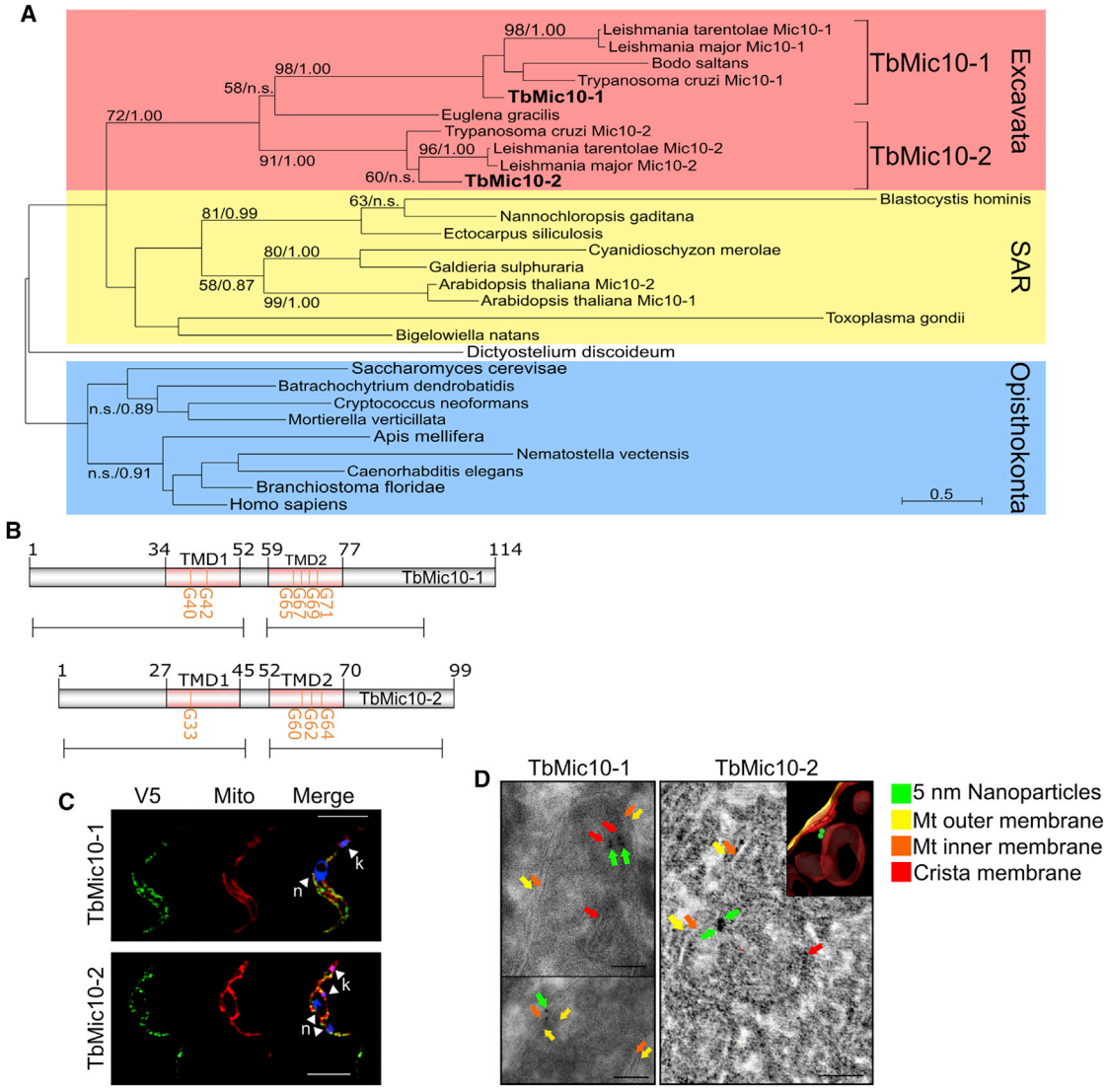

Figure 1. *T. brucei* Has Two Mic10 Paralogs that Localize to Cristae Membranes

(A) Maximum-likelihood tree of Mic10 orthologs from Excavata, SAR, and Opisthokonta. Branches well supported by bootstrap/posterior probabilities are indicated, and "n.s." signifies no support. Scale bar, substitutions/site. Alignment used for the tree is shown in Figure S1A.

(B) Scheme of TbMic10-1 and TbMic10-2. Each transmembrane domain (TMD) is shown in pink with conserved G residues demarked by orange bars. Scale bars indicate LC-MS/MS peptide coverage as in Figure 4B.

(C) Indirect immunofluorescence of TbMic10-1/2. k, kDNA (i.e., mitochondrial genome); n, nucleus. Scale bar, 5 μm.

(D) TbMic10-1-V5 and TbMic10-2-V5 immunogold labeling. Inset, tomography model. Colored arrow key is on right. Scale bars, 50 nm.

See also Video S1.

and/or subcomplexes migrating at ~440 and ~200 kDa (Figure 3A). To immunocapture proteins interacting with TbMic10-1/2, we used TbMic10-1/2-V5 as affinity handles in the *T. brucei* 927 strain. Solubilized hypotonically isolated mitochondria (Figure 3B) were incubated with mouse α-V5 antibody cross-linked to Protein G Dynabeads to immunoprecipitate (IP) the tags. After extensive washing, eluted proteins that coIP with TbMic10-1/2 were trypsinized and identified by liquid chromatography-tandem mass spectroscopy (LC-MS/MS). A mock IP was done with mitochondria from the parental cell line without V5 epitope to discriminate any non-specific binding to the anti-body-bead adduct. TbMic10-1/2-V5 IPs performed in triplicate invariably isolated the same complement of 11 proteins (named using the established MICOS nomenclature) [28], none of which were detected in the mock control (Figure 3C; Data S1A and S1B). All the identified subunits exhibited high peptide coverage (Figure 4B).

These interactions were verified by IP of the subunit we designated TbMic60 (explained in the next section), which was reciprocally tagged with a C-terminal hemagglutinin (HA) epitope. LC-MS/MS analysis revealed the same complement of TbMICOS subunits in triplicate TbMic60 IPs (Figure 3C; Data S1C). The

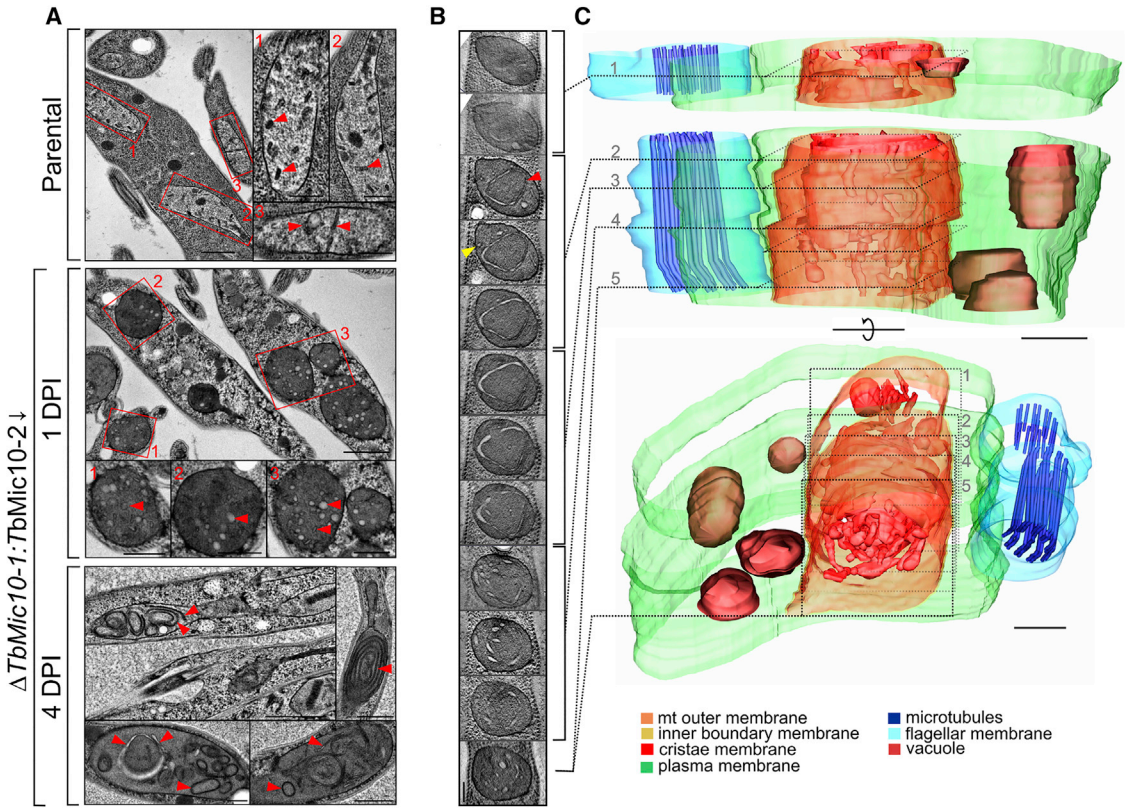

Figure 2. Simultaneous TbMic10-1/2 Ablation Results in Altered Cristae

(A) Representative TEM images from parental and *ΔTbMic10-1*/TbMic10-2↓ 1 and 4 days post-induction (DPI) *T. brucei*. Insets from the former two samples indicate close ups of the boxed and numbered mitochondria in the main images. Scale bars, 1 μm and 500 nm (insets). Representative cristae are indicated by red arrowheads. See also Figure S2.

(B) Serial TEM cryosections of *ΔTbMic10-1*/TbMic10-2↓ 4 DPI. Red and yellow arrows point to crista and inner mitochondrial membranes, respectively. Scale bars, 200 μm.

(C) 3D reconstruction of serial TEM cryosections in (B). Approximate location of sections is numbered and points to its respective section in (B). Key is on bottom. Scale bars, 200 μm.

See also Video S2.

only significant difference was detection of a single peptide from TbSAM50.

TbMICOS composition was also studied in the *T. brucei* 427 strain using a stable isotope labeling by/with amino acids in cell culture (SILAC)-based approach. Four cell lines expressing epitope-tagged versions of putative MICOS subunits TbMic10-1, TbMic10-2, TbMic20, and TbMic34 were subjected to IP using anti-tag antibodies (Figure 3D). The eluted proteins from a mixture of differentially labeled cells either expressing or lacking the tagged bait protein were analyzed by quantitative MS in triplicate to determine protein abundance ratios. In these four IPs, a set of proteins was recovered that were enriched >5-fold. Strikingly, this set was essentially identical to the one recovered in the 927 strain, with the difference of TbMic75 and TbSAM50 not being detected (Figures 3E–3G). However, TbSAM50 was enriched 2.6-fold in the TbMic10-2 IP.

Thus, by using two different IP protocols of 5 different baits in two *T. brucei* strains, we observe the same set of 9 proteins (Figure 4A). This result provides strong evidence that they constitute TbMICOS subunits. To further investigate this hypothesis, each candidate was C-terminally HA-tagged *in situ* in the 927 strain already bearing TbMic10-V5, except TbSAM50, which was N-terminally tagged. TbMic75 was not amenable to tagging and, given its absence in SILAC-IPs, was not pursued further. All TbMICOS subunits plus TbSAM50 were confirmed to assemble into the >1-MDa complex (Figure S3), consistent with their interaction as stable subunits of a single complex or an interaction partner in the case of Sam50.

TbMICOS Coincides with Cristae and Contains Novel Subunits

We determined whether TbMICOS subunit expression levels coincide with the occurrence of cristae via two high-throughput SILAC LC-MS/MS studies comparing the *T. brucei* PS and BS proteomes [29, 30] (Figure 4A). In at least one of these studies, most TbMICOS subunits are more expressed in PS compared to BS, the latter of which lack cristae. Intriguingly, TbMic17 is the sole exception, reported to be downregulated in PS.

Most TbMICOS subunits are well conserved among kinetoplastids (Figure 4A), which agrees with their presumptive association with such basic structures as cristae. Only *B. saltans* lacks

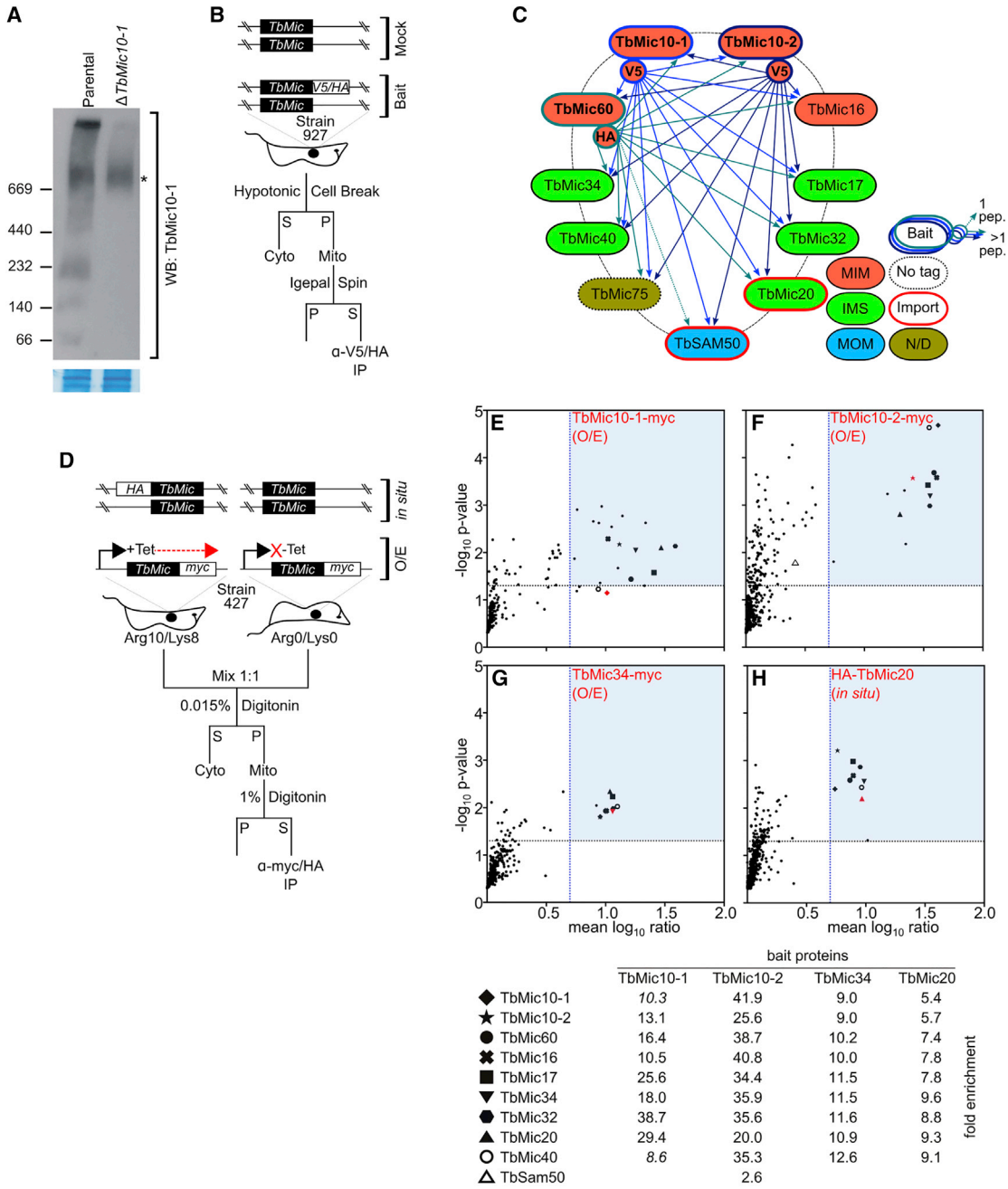

Figure 3. TbMICOS Subunit Composition

(A) Blue native (BN)-PAGE resolution of TbMICOS visualized on a western blot (WB) with anti-TbMic10-1 antibody. *, non-specific band. (Lower panel) Coomassie staining of F_1F_O-ATP synthase as a loading control is shown. Native protein size markers are on left.

(B) Scheme of 927 strain IP mitochondrial isolation and solubilization. (Top) Genetic background of parental cell line (mock) and tagged cell lines (bait) is shown. P, pellet; S, supernatant.

(C) Summary of 927 IPs. Affinity handles for TbMic10-1/2 (V5) and TbMic60 (HA) bait proteins point to co-IP proteins. Key is on right; N/D, sub-organellar localization not determined. Mass spectroscopy data used to make scheme are in Data S1.

(D) Scheme of 427 SILAC-IP as in (B), with genetic background of overexpression (O/E) and *in situ* tagged cell lines depicted at the top.

(E–H) SILAC-IP of epitope-tagged TbMic10-1 (E), TbMic10-2 (F), TbMic34 (G), and TbMic20 (H). x axis, the mean Log_{10} enrichment ratios of replicate bait IPs (n = 3), whose data point is marked in red; y axis, the corresponding Log_{10} p values. Blue quadrant highlights proteins that achieved the threshold of both values. Key to data point shape and fold enrichment for each protein is shown at the bottom.

See also Data S2 and Figure S3.

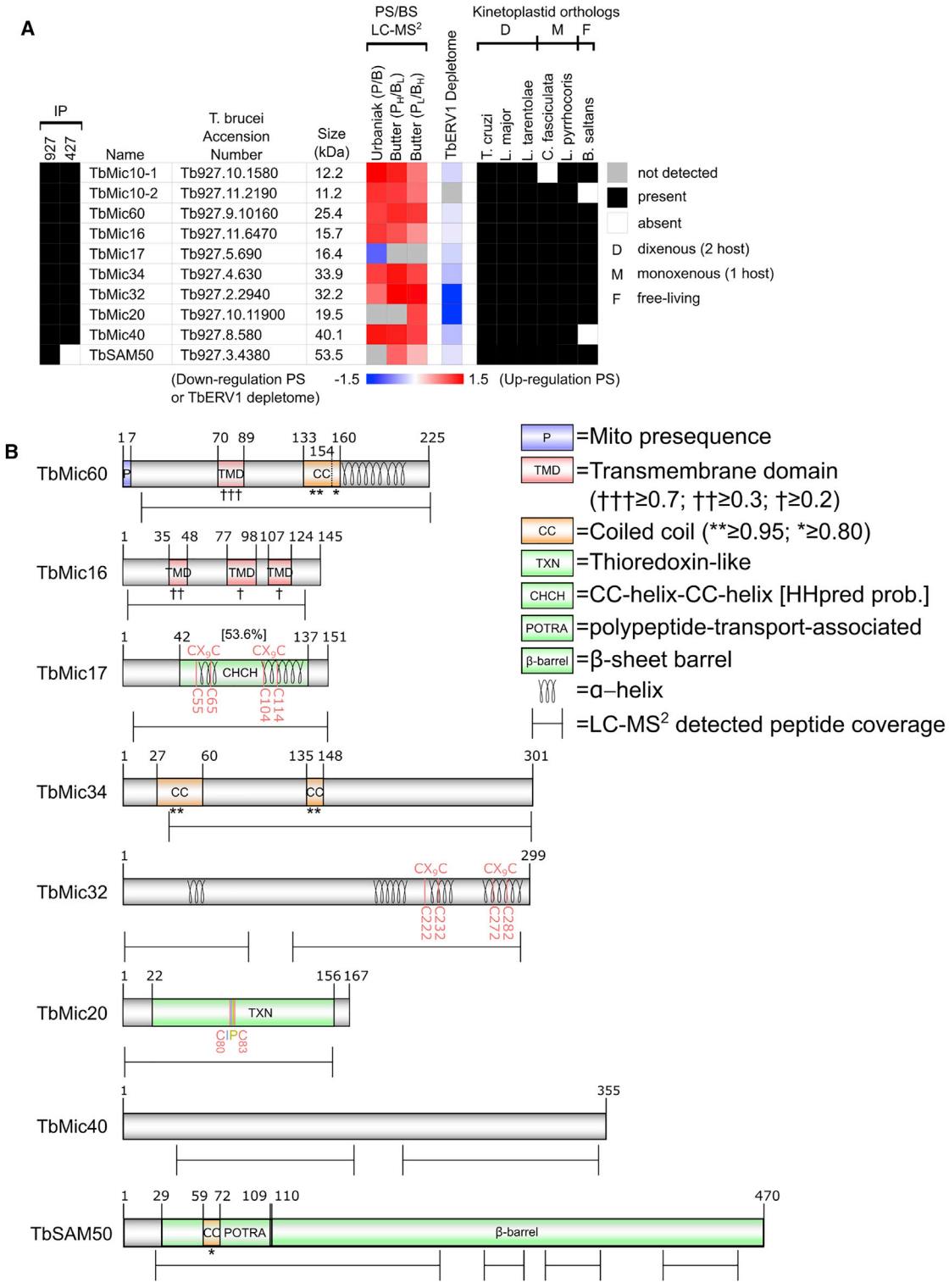

Figure 4. TbMICOS Subunit Analysis

(A) Summary of TbMICOS subunits: presence in IPs; SILAC LC-MS/MS determined expression levels in PS (P) and BS (B) by SILAC proteomics in Urbaniak [29] and Butter [30] studies with labeling indicated in subscripts (H, heavy; L, light); levels in TbERV1 depletome [31]; ortholog presence in other kinetoplastids. Relative protein abundance scale is shown below relevant columns. Key is on right. Accession numbers of kinetoplastid orthologs are in Table S1.

(B) Domain architecture and presence of α helices. Key to color-coding of motifs is on right. Probability scores from CC and TMD prediction software are indicated by * and †, respectively. Scale bars indicate LC-MS/MS peptide coverage as in Figure S1.

See also Figures S1B and S1C.

a homolog of TbMic40. Interestingly, the monoxenous trypanosomatid *Crithidia fasciculata* appears to have lost TbMic10-2.

Because these subunits are restricted to kinetoplastids, we investigated their domain architecture *in silico* to gain insight into their possible function. We designate a 25-kDa protein TbMic60 despite it missing the C-terminal mitofilin domain, which has been thus far this protein family's defining character [1]. However, TbMic60 has the same domain architecture of the N-terminal half of other Mic60 orthologs: a predicted mitochondrial presequence [32] that is consistent with observed LC-MS/MS peptide coverage (Figure S1B); a single TMD; a coiled coil (CC) domain; an α helix interspersed with conserved charged; and aromatic amino acids [33] (Figure S1C).

TbMic16 has 3 predicted TMDs, and TbMic34 has 2 putative CC domains. TbMic17 and TbMic32 have a pair of CX_9C motifs within predicted α helices, an IMS protein signature. TbMic17 has a degenerated CHCH domain that is detected by HHpred structure prediction [34], a feature also found in opisthokont Mic19. Interestingly, TbMic20 is a thioredoxin-like protein, complete with a CIPC motif that may catalyze redox reactions.

Association of TbMICOS with Cristae Membranes

The sub-organellar localization of TbMICOS was undertaken next. To facilitate comparison of all TbMICOS subunits, TbMic10-1/2 were also *in situ* HA tagged. The molecular weight of each tagged protein, with an extra ~5 kDa from the epitope, was confirmed by western blot analysis. The tagged proteins also served as proxies to estimate steady-state levels of TbMICOS subunits (Figure S4A). Consistent with aforementioned high-throughput proteomics data, TbMic17-HA was the least expressed subunit. Also, TbMic60-HA and TbMic34-HA exhibit similar levels (Figure S4B).

Next, hypotonically isolated mitochondria from the tagged TbMICOS cell lines were fractionated into matrix and membrane parts, the latter being further separated into peripheral and integral MIM fractions using an established pipeline [35] (Figure S4C). These fractions were probed with mitochondrial HSP70 [36] as a marker for matrix and peripheral MIM fractions. Expectedly, TbMic10-1-V5 and TbMic10-2-HA ended up in fractions having the integral MIM component prohibitin [37], confirming these are membrane proteins (Figure S4D). As each cell line contained TbMic10-1-V5, it was subsequently used as an integral membrane protein marker. TbMICOS subunit localization agreed with *in silico* predictions: TbMic60 and TbMic16 are integral proteins and the rest are in the MIM periphery (Figure S4D).

The sub-organellar localization of the soluble epitope-tagged TbMICOS subunits and integral subunit topology were subsequently addressed. Mitoplasts derived from these cell lines were subjected to a proteinase K protection assay (Figure S4E). Persistence of the C-terminal epitope indicates its localization in the matrix face of the intact MIM. The presence of matrix HSP70 and degradation of IMS TbERV1 confirmed the functionality of the assay. TbMic10-1-V5 served as a control after its topology had been verified (Figure S4F). In all cases, the C-terminal tag was degraded, indicating presence of the corresponding protein in the IMS.

Then, we asked whether the MICOS subunits are enriched within cristae *in vivo*. To address this question qualitatively, immunogold labeling of HA epitopes was employed in all TbMICOS cell lines, viewed by ET for integral subunits or TEM for the rest. As seen in Figures 5A–5T and Video S1, NPs mostly decorate cristae membranes, with some signal observed at the inner boundary membrane. Quantitative immunogold TEM revealed that HA-binding NPs were concentrated in mitochondria in comparison with the parental cell line lacking the epitope (Figure 5U). In all cases except TbMic20, more than half of NPs label cristae and all show significant inner boundary membrane localization (Figure 5V). This pattern is in contrast to the parental cell line, in which most NPs associate with undefined mitochondrial structures. Interestingly, HA-binding NPs often appear in clusters (Figures 5A–5D), suggesting a multimeric stoichiometry of the tagged protein within TbMICOS. This phenomenon was quantified by NP pairs that were <30 nm apart, revealing that most tagged subunits formed clusters with median ~10-nm distances (Figure 5W). Such clustering was vastly underrepresented in the negative control parental cells. In summary, we have shown that the TbMICOS subunits localize to cristae membranes in a way suggesting their multimerization.

Depletion of TbMICOS Subunits Alters Cristae

After establishing that TbMICOS localizes to cristae membranes, we asked whether some subunits have a role in shaping cristae, as was shown by concurrent ablation of TbMic10-1/2. Each cell line was transfected with a construct for inducible RNAi targeting a specific TbMICOS subunit or TbSAM50. An HA-tagged copy of each subunit allowed us to follow silencing of the target proteins using α-HA antibody and a consequent effect on TbMic10-1-V5. Over 6 days of RNAi induction, each cell line exhibited downregulation of its target subunit compared to HSP70 (Figure 6A).

Afterward, we examined whether depletion of each TbMICOS subunit compromised cell growth in a glucose-rich medium. We observed that all RNAi knockdowns except TbMic16 resulted in slower growth compared to mock-treated cell lines, usually 2 or 3 dpi (Figure 6B). This result was unexpected because growth was not inhibited in either *ΔTbMic10-1*:TbMic10-2↓ *T. brucei* (Figure S2C) or in MICOS yeast mutants grown on fermentable substrates [39]. Cell growth in glucose-poor medium, in which PS proliferation relies on OXPHOS [40], was not more severely affected (Figure S5A). Therefore, almost all TbMICOS subunits are essential for normal growth, irrespective of the mitochondrial bioenergetic state.

Cristae morphology was then observed in ultrathin cryosections of cells depleted of individual TbMICOS subunits at RNAi time points just before acute growth arrest (Figure S5B). TbMic40 RNAi stands out due to massive mitochondrial blebbing. TbMic60 and TbMic20 RNAi silencing exhibited phenotypes resembling those of *ΔTbMic10-1*:TbMic10-2↓4 dpi (Figure 2), with elongated cristae assuming an arc-like or circular morphology. To quantify this phenomenon, we measured cristae lengths of selected RNAi-silenced subunits, *ΔTbMic10-1*:TbMic10-2↓ and the parental strain (Figure 6C). These results correlated with qualitative observations, in which TbMic60 and TbMic20 RNAi displayed elongated cristae on par with *ΔTbMic10-1*:TbMic10-2↓. Furthermore, downregulation of TbMic34 resulted in a lesser degree of elongation similar to that of *ΔTbMic10-1*:TbMic10-2↓ 1 dpi. Other morphological parameters were also measured. *ΔTbMic10-1*:TbMic10-2↓ and TbMic60 RNAi exhibited an increase in mitochondrial area

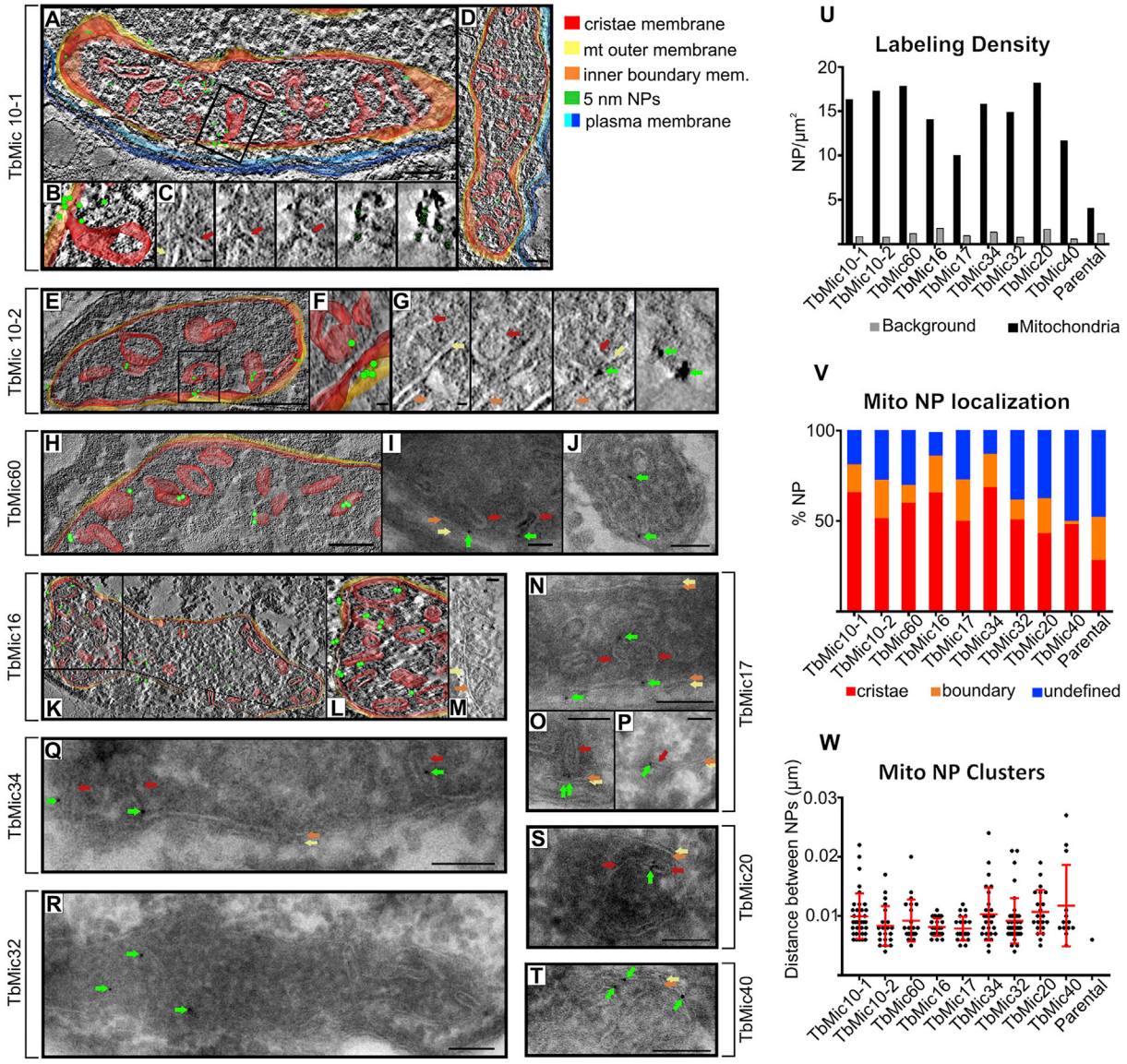

Figure 5. TbMICOS Localization in Cristae Membranes

(A–T) Representative electron tomography (A–M) and transmission electron microscopy (N–T) of subunits indicated on left (A–M, Q, and R) and right (N–P, S, and T) of brackets. Key on upper right classifies colors of structures (membranes and nanoparticles [NPs]) or arrows pointing to structures. C and G show electron tomography tilt series. Scale bars, 200 µm. See also Video S1.

(U) Labeling density of NPs in mitochondria (black bars) or background (gray bars). Statistical analyses of the labeling density by measuring relative labeling index [38] are given in Table S2, which contains total surface areas of mitochondria and background (i.e., rest of cell) examined in all analyses in (U)–(W).

(V) Localization of NPs within mitochondrial subcompartments. Red, cristae; orange, inner boundary membrane; blue, undefined.

(W) NP cluster analysis. Each dot represents measured distance (y axis) between 2 NPs. Median and interquartile range of these distances are in red. See also Figure S4.

(Figure 6D), correlating with the appearance of elongated cristae. There is a statistically significant increase in cristae per mitochondria in *ΔTbMic10-1*:TbMic10-2↓, and TbMic32 and TbMic20 displayed less of them, as compared to the parental control (Figure 6C). We have thus established that a subset of TbMICOS subunits, including TbMic60, shapes cristae.

Because the effect of TbMICOS ablation on *T. brucei* growth does not seem to correlate with altered cristae morphology, an effect on proteins of different mitochondrial compartments was examined in the RNAi cells (Figure 6A). Downregulation of all TbMICOS subunits except TbMic17 exhibited a subsequent depletion of TbMic10-1-V5. The voltage-dependent ion channel (VDAC) [41] was only affected upon TbSAM50 ablation. F_OF_1-ATP synthase β subunit was not decreased in any of the cell lines. However, we observed an unexpected significant drop in the abundance of the IMS protein TbERV1 [42] following RNAi against TbMic16, TbMic32, and TbMic20. To summarize, TbMic10-1 stability seems to depend on the presence of the

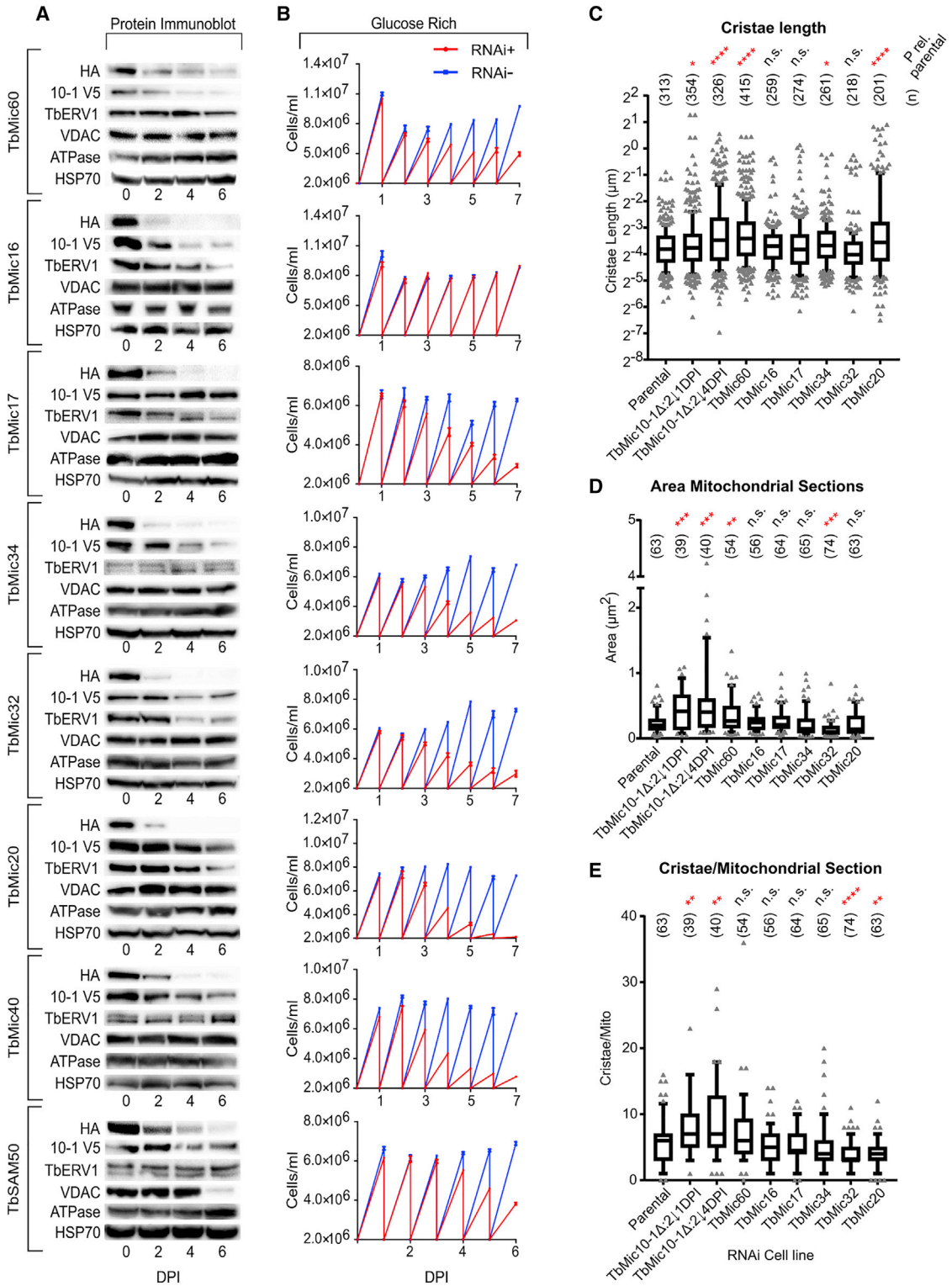

Figure 6. TbMICOS Subunit RNAi Phenotypes

(A) Immunoblot of RNAi cell lines (left of brackets) with antibody indicated on left. Days post-induction (DPI) are shown below panel.

(B) Measurement of TbMICOS RNAi growth in glucose-rich medium in which cells are diluted to 2 × 10^6 cells/mL every day (n = 3; error bars, SD). Cell density, y axis; DPI, x axis.

(C–E) Cristae properties in indicated RNAi cell lines.

(C) Cristae length measurement; y axis $\log_2$ transformed.

(legend continued on next page)

other TbMICOS subunits plus TbSAM50. Moreover, TbERV1 decreases upon depletion of some TbMICOS subunits, an intriguing phenomenon we further explored.

Thioredoxin-like TbMic20 Affects the Import of IMS Proteins

The downregulation of the IMS protein TbERV1 upon RNAi silencing of 3 TbMICOS subunits suggested that the complex may participate in the MIA pathway. TbERV1 is a key component of MIA, as evidenced by its knockdown in PS resulting in IMS protein downregulation [31]. Indeed, 2 of the 3 proteins affecting TbERV1 in our study, TbMic20 and TbMic32, were among those in the TbERV1 depletome (Figure 4A). However, an enzyme catalyzing IMS import in trypanosomes, in a way akin to opisthokont Mia40, remains unidentified [43].

We turned our attention to TbMic20 as a possible functional analog of Mia40. Along with it being affected by TbERV1 ablation, this hypothesis is supported by it having elements as a thioredoxin-like protein that could facilitate oxidative folding of $CX_{3,9}C$ IMS proteins. A TbMic20 homology model templated onto thioredoxin predicts that the CIPC reaction center occurs on a loop adjacent to an α helix, resulting in a structural motif similar to that of the human Mia40 CPC reaction center [22] (Figure S6A).

To address empirically whether TbMic20 is involved in MIA, we tested whether its depletion would result in reduced IMS protein abundance and thus phenocopy TbERV1 RNAi. Equal amounts of mitochondria were isolated from duplicate uninduced and 4 dpi TbMic20 RNAi cells. Proteins were extracted with ionic detergent, and their trypsin-derived peptides were labeled with tandem mass tags for sample discrimination after mixing them in equal parts before LC-MS/MS. In parallel, the same experiment was done for TbMic60.

A $\geq$1.6-fold threshold in both biological duplicates was set for detection of up- and downregulated proteins (Data S2A and S2B [TbMic20] and S2C and S2D [TbMic60]). Verified and predicted IMS proteins comprised 51% of the TbMic20 depletome (Figures 7A and S6B). Of these, over half overlap with those from the TbERV1 depletome (Figures 7A and 7B) [31]. Strangely, a ubiquinol-cytochrome *c* reductase that was decreased in the TbERV1 depletome was reproducibly the most upregulated protein upon TbMic20 RNAi silencing (Figures 7C and S6B). The other TbMic20 depletome IMS proteins belong to two categories: those identified by homology or experimentally (IMS) and those predicted to have a twin $CX_{3,9}C$ motifs (CxC). Notably, TbERV1 was not significantly affected by TbMic20 depletion 4 dpi, indicating that the phenotype is a direct effect (Figure 7C). Furthermore, such an effect on IMS proteins was not observed in the 4 dpi TbMic60 depletome analyzed in parallel. Thus, we provide evidence that TbMic20 participates in MIA.

Many of the affected IMS proteins are annotated as respiratory chain complex assembly factors (Figures 7C and S6B). Two of the most significantly downregulated proteins in the TbMic20 depletome are the respiratory complex III Rieske iron-sulfur protein and a complex I subunit (Figures S6B and S7). Given that cristae membranes are enriched in OXPHOS complexes [3], we interrogated the TbMic20 depletome for a preferential effect on respiratory chain components over matrix proteins, using the annotation of Zíková et al. [25]. Indeed, respiratory chain subunits were generally decreased in the 4 dpi TbMic20 depletome, and no such effect occurs in that of TbMic60 (Figure S7). Only the aforementioned pair of complex I and III subunits crossed the 1.6-fold threshold, suggesting the decline in the other OXPHOS subunits is a secondary effect of IMS-localized $CX_{3,9}C$ OXPHOS assembly factor depletion. Furthermore, the TbMic20-depletome more severely affects OXPHOS complex subunits, with the exception of complex II, than matrix proteins (Figure 7D). This finding suggests that TbMic20 association with cristae may facilitate population of its membrane with OXPHOS components.

We also examined how TbMic20 and TbMic60 RNAi depletion affected the TbMICOS subunits (Figure 7C). Although not significant, TbMic34, TbMic32, and TbMic40 were most affected by TbMic20 ablation. Among the 32 proteins downregulated by $\geq$1.6-fold in the TbMic60 RNAi cells are the target and TbMic16. TbMic10-1 appeared to be affected as well, confirming aforementioned western blot data (Figure 6A). Whether this differential effect of TbMic20 and TbMic60 depletion reflects a subcomplex architecture, as has been reported for yeast MICOS [39, 44, 45], remains to be determined.

DISCUSSION

Defining Conserved Features of MICOS

This study represents the first isolation and characterization of a MICOS complex outside of opisthokonts. As a highly diverged excavate unrelated to opisthokonts, *T. brucei* is well positioned to help identify highly conserved and relaxed features of MICOS that mediate CJ biogenesis and cristae shaping. The fundamental architecture of MICOS appears to be conserved, with novel supernumerary subunits attached to a MIM embedded core represented by Mic10 and Mic60 [11–13], albeit with diverged qualities that will be discussed later. Furthermore, some TbMICOS subunits appear to be multimeric, as has been observed in opisthokonts.

The association of MICOS with ancient Sam50 is conserved. The yeast Mic60 mitofilin domain mediates interaction with Sam50 [17–19] to form the even larger mitochondrial IMS bridging complex [2, 46]. Despite TbMic60 lacking the mitofilin domain, this interaction between TbMICOS and TbSAM50 was confirmed by its co-IP with TbMic10-1/2 and TbMic60. Furthermore, TbSAM50 assembles in a >1-MDa complex that was also observed in TbMICOS. Finally, TbSAM50 RNAi leads to TbMic10-1 downregulation.

In yeast, Cox17 and Aim24 have been shown to be peripheral MICOS interaction partners [47, 48]. It is possible that some of the TbMICOS subunits whose RNAi silencing does not yield the scored elongated cristae phenotype may represent such auxiliary factors. However, a counterargument to this idea is the tight association of the 9 TbMICOS subunits in 7 IPs performed under 2

(D) Mitochondrial section area measurement.

(E) Cristae per mitochondrial section in RNAi cell lines.

Boxplots show median and interquartile range. Whiskers demark data points in the 10–90 percentiles. Statistical significance of differences between each RNAi cell line and parental control is shown on top with population size (n): ****p < 0.0001; ***p < 0.001; **p < 0.01; *p < 0.05; n.s., not significant. See also Figure S5.

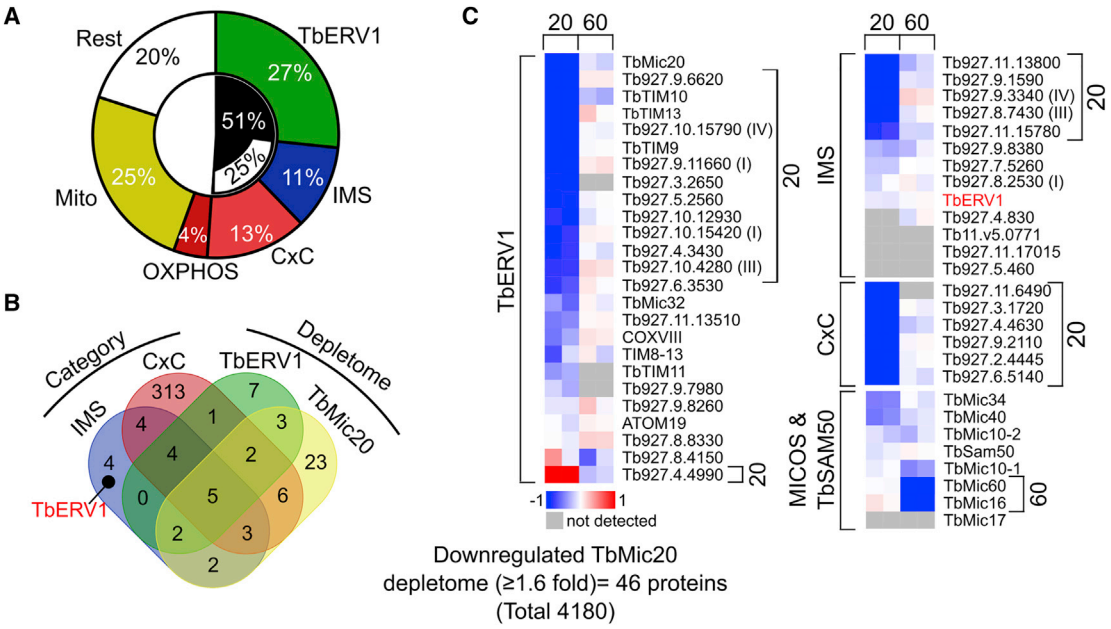

Downregulated TbMic20 depletome (≥1.6 fold)= 46 proteins (Total 4180)

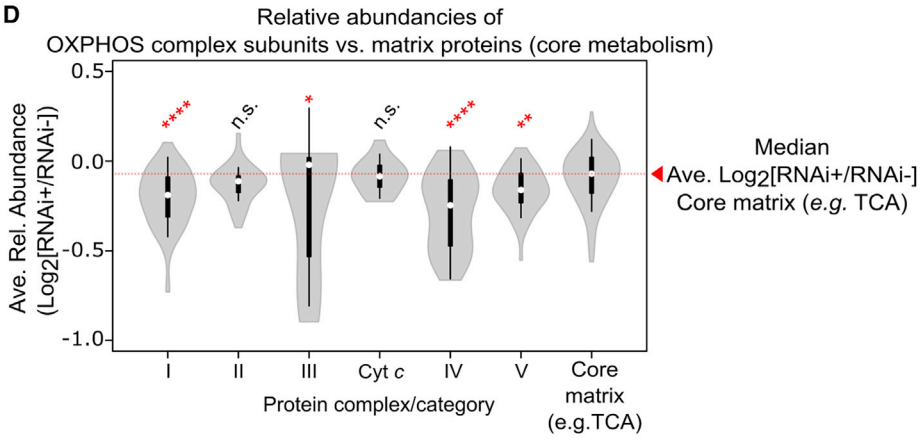

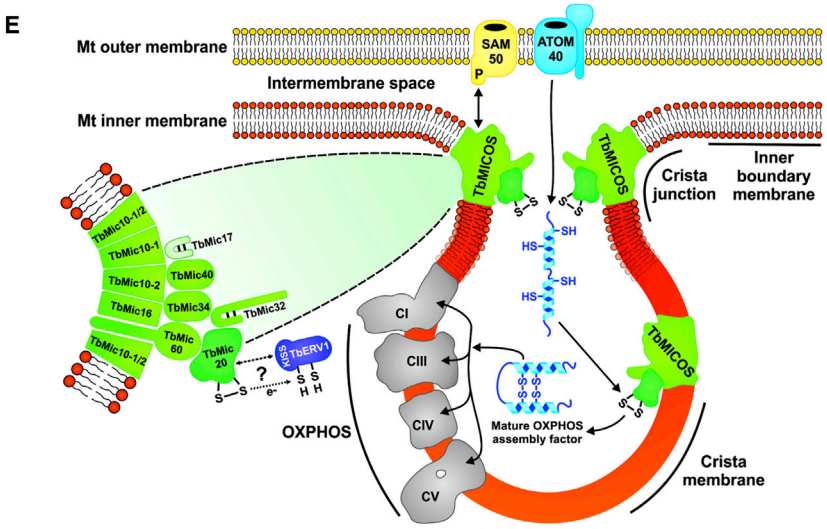

(legend on next page)

conditions. This is similar to the interconnection of yeast MICOS subunits upon their initial biochemical purification in 3 studies, none of which contained later identified peripheral proteins [8–10]. Furthermore, RNAi depletions of some human MICOS subunits also do not yield altered cristae [46], a similar result to ours. In the case of TbMICOS, perhaps the lack of the scored phenotype upon specific subunit depletion may be due to their functional redundancy under the examined conditions, as has been observed in attempts to delete each *TbMic10* paralog individually. Nevertheless, we cannot completely rule out the likelihood that some of the identified TbMICOSs are auxiliary factors, although we believe this to be a remote possibility.

Novel Features of TbMICOS

Although lacking the C-terminal mitofilin domain, TbMic60 retains the domain architecture of the N-terminal half of the protein, comprising of a mitochondrial presequence, single TMD, and CC domain [1, 2], that justifies its designation as a Mic60 ortholog. The α-proteobacterial ortholog of Mic60 also contains these elements, minus the presequence. Interestingly, the β- and γ-proteobacterial HemX protein, whose gene is syntenic to α-proteobacterial *Mic60* [2], bears these elements. Yet HemX lacks a mitofilin domain, setting a naturally occurring precedent for its absence between distantly related but still structurally conserved homologs. However, although bacterial Mic60 has been shown to bend membranes *in vitro* [15], such an activity remains to be determined for HemX. Still, the mitofilin domain is unnecessary for membrane bending, an activity mediated instead by the CC-domain-trailing α helix interspersed with aromatic and charged amino acids [33], a feature found in TbMic60. Finally, TbMic60 ablation exhibits one of the strongest cristae morphology phenotypes, analogous to the severity of Δ*Mic10* and Δ*Mic60* on yeast cristae [8, 10].

It is plausible that another TbMICOS subunit may assume the missing mitofilin domain's role, with TbMic34 being a top candidate. HA-tagged TbMic60 and TbMic34 have similar expression levels, which is compatible with their stoichiometric relationship. Furthermore, they are the only two subunits with CC domains, which could allow them to form an ~60-kDa heterodimer. Finally, TbMic34 RNAi caused a perceptible cristae-elongation phenotype, albeit to a lesser extent than observed upon TbMic60 silencing.

Uniquely, most trypanosomatid genomes encode two TbMic10 paralogs. They are functionally redundant in cultured PS *T. brucei*, because an obvious phenotype occurs only when both paralogs are ablated simultaneously. We speculate that the two isoforms help to regulate cristae formation in trypanosomatids with complicated life cycles, exemplified by cristae emergence during differentiation of *T. brucei* from BS to PS [25]. Concordantly, a single Mic10 ortholog is found in *B. saltans*, a free-living kinetoplastid, and the monoxenous trypanosomatid *C. fasciculata*, both having simpler life cycles.

Although simultaneous ablation of TbMic10-1/2 causes CJ loss and some TbMICOS subunits were detected at CJs, we mostly observe TbMICOS distributed throughout the cristae membrane. This localization is in contrast to the CJ enrichment of yeast MICOS [8–10, 39]. This may be due to the difficulty of capturing *T. brucei* CJs in cryosections. However, we favor the interpretation that TbMICOS is distributed throughout discoidal cristae for two reasons. The first involves the yeast lamellar cristae biogenesis pathway, requiring fusion of MIMs from two mitochondria [49]. MICOS was proposed to participate in this process by halting complete fusion of the MIM at CJs, which would otherwise lead to the detached cristae seen in Δ*MICOS* mutants. As kinetoplastids have a single mitochondrion, this cristae formation pathway may be absent, thus explaining the broad distribution of TbMICOS. The second reason is related to the thioredoxin-like TbMic20.

TbMICOS Is Involved in Intermembrane Space Protein Import

Until this study, an analog of Mia40, the central MIA enzyme in opisthokonts [20, 21] that is widely distributed throughout eukaryotes [50], has remained unidentified in *T. brucei* [42, 43]. We have serendipitously found a putative functional analog, TbMic20, among the stably interacting TbMICOS subunits. Its CIPC motif could execute disulfide bridge formation in IMS precursors by a similar mechanism as the Mia40 CPC reaction center [22]. Although more evidence is needed to support TbMic20 as the genuine MIA catalyst arising from convergent evolution, the fact that its depletion results in a preferential decrease of IMS proteins points to this conclusion.

In yeast, the sulfhydryl oxidase Erv1 directly binds Mia40 during IMS import [51]. However, TbERV1 is absent in all TbMICOS

Figure 7. TbMic20 RNAi Affects IMS Proteins

(A) Summary of downregulated proteins (≥1.6-fold threshold) in TbMic20 depletome. CXC, predicted $CX_{3,9}C$ pair containing proteins; IMS, experimentally or by homology identified IMS proteins; Mito, experimentally or by homology identified mitochondrial proteins; OXPHOS, subunits of respiratory chain; Rest, proteins that do not fall into these categories; TbERV1, depletome proteins. See also Figure S6.

(B) Venn diagram comparing TbMic20 and TbERV1 depletomes using category definitions as in (A).

(C) Heatmaps of log_2-transformed relative abundancies in TbMic20 (20) and TbMic60 (60) depletomes organized into categories as in (A). Brackets indicate proteins achieving the ≥1.6-fold threshold. Roman numerals in parentheses indicate OXPHOS complex component and/or assembly factor. Scale of relative protein abundance is on bottom of TbERV1 column.

(D) Violin plot of the log_2-transformed relative abundancies of respiratory chain complexes I–V, cytochrome-*c*-related proteins, and core matrix metabolism proteins (core), such as TCA cycle enzymes. Median downregulation for each protein population is marked by white circle; thick lines indicate the interquartile range of downregulated proteins and thin lines extend 1.5 times from the quartiles. Red dotted line across graph demarks median value for relative abundance of core proteins. Above each plot is the statistical significance of the different categories relative to the core group as indicated (****$p < 0.0001$; ***$p < 0.001$; **$p < 0.01$; *$p < 0.05$; n.s., not significant). Related to Figure S7.

(E) Proposed role of TbMICOS in cristae biogenesis. Mechanistic details are described in Discussion. IMS proteins are shown with blue α helices and thiols. Respiratory chain complexes (C) I and III–V are in gray. Inset depicts the theoretical composition of TbMICOS with undefined subunit stoichiometry. Faint color of TbMic17 reflects its low abundance in PS *T. brucei.* Possible interaction with TbERV1 bearing KISS domain is also depicted. P, Sam50 POTRA domain. See also Data S2.

preparations and reciprocally TbERV1 IP did not immunocapture TbMICOS [43]. However, TbERV1 localizes within discoidal cristae [43], as does TbMic20. Furthermore, TbERV1 has a "kinetoplastid-specific second" (KISS) domain [52], which may be an adaptation for binding another oxidoreductase besides Mia40 and/or stabilize the TbERV1 dimer when it is not transiently interacting with TbMic20.

TbMic20 RNAi not only results in a decrease of IMS proteins but also causes cristae elongation. This observation encapsulates our current model that TbMICOS serves as a hub for cristae shaping and IMS protein import (Figure 7E). TbMICOS via TbMic20 facilitates the oxidative folding of $CX_{3,9}C$-containing OXPHOS components, including OXPHOS assembly factors. TbMICOS distribution throughout cristae membranes allows the concentration of mature assembly factors in proximity to this membrane. In turn, this mechanism aids the population of cristae membrane with OXPHOS complex subunits that require these IMS proteins. TbMICOS also maintains CJs, anchoring cristae to the MOM via TbSAM50 interaction, bringing the crista lumen closer to the ATOM protein import pores [53], through which IMS protein precursors are translocated.

TbMICOS subunit depletion impairs *T. brucei* growth even under conditions in which energy generation occurs independently of OXPHOS. Thus, we propose that this is ultimately a consequence of mitochondrial import disruption. Indeed, many MIA substrates are involved in mitochondrial biogenesis, such as the small Tim chaperones [54]. Furthermore, the ATOM complex, the entry gate for nearly all proteins into the organelle, is also essential for *T. brucei* grown in ample glucose [53].

The Evolutionary Cell Biology of MICOS

We have explored the composition and function of MICOS in *T. brucei* to obtain much needed data about how this complex works outside of opisthokonts. Ultimately, our goal has been to better understand the MICOS complex by gaining insight into the evolutionary constraints that shape it. We confirm the hypothesis that the core function of MICOS in diverged eukaryotes is the maintenance of CJs, cristae shaping, and mediating MOM and MIM contacts. However, we also uncovered many surprising novelties that demonstrate MICOS has the potential to follow diverse evolutionary paths to adapt to different cellular contexts. Among them are TbMic60's lacking the conserved mitofilin domain and TbMic10 duplication into two distinct proteins. Yet most surprising is the presence of a thioredoxin-like TbMICOS subunit, which may allow MICOS to participate in IMS protein import. This activity extends the currently accepted functional model of MICOS, helping OXPHOS complex insertion into cristae membranes. It remains to be seen whether these novel TbMICOS properties are restricted to trypanosomatids or have a wider distribution in eukaryotes, indicating that opisthokont MICOS may actually represent the outlier.

STAR★METHODS

Detailed methods are provided in the online version of this paper and include the following:

- KEY RESOURCES TABLE
- CONTACT FOR REAGENT AND RESOURCE SHARING
- EXPERIMENTAL MODEL AND SUBJECT DETAILS
- METHOD DETAILS
  - Generation of T. brucei transgenic cell lines
  - T. brucei growth measurements
  - Mitochondria isolation and sub-fractionation
  - Antibody crosslinking to protein G Dynabeads
  - Immunoprecipitations
  - Mass spectrometry
  - LC-MS^2 analysis of peptides
  - SILAC proteomics
  - Proteinase K protection assay
  - Transmission electron microscopy
  - Bioinformatic analysis
- QUANTIFICATION AND STATISTICAL ANALYSIS
  - Analysis of immunogold and RNAi transmission electron microscopy data
  - Analysis of TbMic20 and TbMic60 depletome data
- DATA AND SOFTWARE AVAILABILITY

SUPPLEMENTAL INFORMATION

Supplemental Information includes seven figures, three tables, two videos, and two data files and can be found with this article online at https://doi.org/10.1016/j.cub.2018.09.008.

ACKNOWLEDGMENTS

We thank Jan Mani and Julia Bruggisser (University of Bern) for help at early phases of the project, Andreas Reichert (University of Düsseldorf) for initial consultation, Bettina Knapp for technical assistance with SILAC LC-MS/MS, and Aleš Horák for advice on phylogenetics. Support from the Czech Grant Agency (16-18699S to J.L. and 17-24036S to H.H.), ERC CZ (LL1601) to J.L., and ERD Funds (project OPVVV 16_019/0000759) to H.H. and J.L. is acknowledged. A.S. was supported by Swiss National Science Foundation grant 175563 and NCCR "RNA & Disease." B.W. was supported by ERC Consolidator Grant 648235, the Deutsche Forschungsgemeinschaft (Research Training Group RTG 2202), and Excellence Initiative of the German Federal and State Governments (EXC 294 BIOSS). Support from MEYS CR is acknowledged by M.V. and T.B. for the Czech BioImaging grant (LM2015062) and D.P. and Z.Z. for the CIISB research infrastructure project (LM2015043) and CEITEC 2020 (LQ1601) for supporting LC-MS/MS measurements at the Proteomics Core Facility, CEITEC, Masaryk University.

AUTHOR CONTRIBUTIONS

M.V., B.S., and H.H. designed the study. I.K., M.V., B.S., L.R.C., J.H., T.B., D.P., C.E., H.B., S.O., and H.H. performed the experiments. I.K., M.V., B.S., T.B., D.P., S.O., A.S., and H.H. analyzed the data. B.S., M.V., D.P., B.W., Z.Z., A.S., J.L., and H.H. wrote the paper.

DECLARATION OF INTERESTS

The authors declare no competing interests.

Received: June 25, 2018
Revised: August 2, 2018
Accepted: September 4, 2018
Published: October 25, 2018

REFERENCES

1. Muñoz-Gómez, S.A., Slamovits, C.H., Dacks, J.B., Baier, K.A., Spencer, K.D., and Wideman, J.G. (2015). Ancient homology of the mitochondrial contact site and cristae organizing system points to an endosymbiotic origin of mitochondrial cristae. Curr. Biol. *25*, 1489–1495.

2. Huynen, M.A., Mühlmeister, M., Gotthardt, K., Guerrero-Castillo, S., and Brandt, U. (2016). Evolution and structural organization of the mitochondrial contact site (MICOS) complex and the mitochondrial intermembrane space bridging (MIB) complex. Biochim. Biophys. Acta *1863*, 91–101.
3. Vogel, F., Bornhövd, C., Neupert, W., and Reichert, A.S. (2006). Dynamic subcompartmentalization of the mitochondrial inner membrane. J. Cell Biol. *175*, 237–247.
4. Davies, K.M., Anselmi, C., Wittig, I., Faraldo-Gómez, J.D., and Kühlbrandt, W. (2012). Structure of the yeast F1Fo-ATP synthase dimer and its role in shaping the mitochondrial cristae. Proc. Natl. Acad. Sci. USA *109*, 13602–13607.
5. Davies, K.M., Strauss, M., Daum, B., Kief, J.H., Osiewacz, H.D., Rycovska, A., Zickermann, V., and Kühlbrandt, W. (2011). Macromolecular organization of ATP synthase and complex I in whole mitochondria. Proc. Natl. Acad. Sci. USA *108*, 14121–14126.
6. Cogliati, S., Enriquez, J.A., and Scorrano, L. (2016). Mitochondrial cristae: where beauty meets functionality. Trends Biochem. Sci. *41*, 261–273.
7. Kühlbrandt, W. (2015). Structure and function of mitochondrial membrane protein complexes. BMC Biol. *13*, 89.
8. Harner, M., Körner, C., Walther, D., Mokranjac, D., Kaesmacher, J., Welsch, U., Griffith, J., Mann, M., Reggiori, F., and Neupert, W. (2011). The mitochondrial contact site complex, a determinant of mitochondrial architecture. EMBO J. *30*, 4356–4370.
9. Hoppins, S., Collins, S.R., Cassidy-Stone, A., Hummel, E., Devay, R.M., Lackner, L.L., Westermann, B., Schuldiner, M., Weissman, J.S., and Nunnari, J. (2011). A mitochondrial-focused genetic interaction map reveals a scaffold-like complex required for inner membrane organization in mitochondria. J. Cell Biol. *195*, 323–340.
10. von der Malsburg, K., Müller, J.M., Bohnert, M., Oeljeklaus, S., Kwiatkowska, P., Becker, T., Loniewska-Lwowska, A., Wiese, S., Rao, S., Milenkovic, D., et al. (2011). Dual role of mitofilin in mitochondrial membrane organization and protein biogenesis. Dev. Cell *21*, 694–707.
11. Kozjak-Pavlovic, V. (2017). The MICOS complex of human mitochondria. Cell Tissue Res. *367*, 83–93.
12. Wollweber, F., von der Malsburg, K., and van der Laan, M. (2017). Mitochondrial contact site and cristae organizing system: A central player in membrane shaping and crosstalk. Biochim. Biophys. Acta *1864*, 1481–1489.
13. Rampelt, H., Zerbes, R.M., van der Laan, M., and Pfanner, N. (2017). Role of the mitochondrial contact site and cristae organizing system in membrane architecture and dynamics. Biochim. Biophys. Acta *1864*, 737–746.
14. Barbot, M., Jans, D.C., Schulz, C., Denkert, N., Kroppen, B., Hoppert, M., Jakobs, S., and Meinecke, M. (2015). Mic10 oligomerizes to bend mitochondrial inner membranes at cristae junctions. Cell Metab. *21*, 756–763.
15. Tarasenko, D., Barbot, M., Jans, D.C., Kroppen, B., Sadowski, B., Heim, G., Möbius, W., Jakobs, S., and Meinecke, M. (2017). The MICOS component Mic60 displays a conserved membrane-bending activity that is necessary for normal cristae morphology. J. Cell Biol. *216*, 889–899.
16. Bohnert, M., Zerbes, R.M., Davies, K.M., Mühleip, A.W., Rampelt, H., Horvath, S.E., Boenke, T., Kram, A., Perschil, I., Veenhuis, M., et al. (2015). Central role of Mic10 in the mitochondrial contact site and cristae organizing system. Cell Metab. *21*, 747–755.
17. Bohnert, M., Wenz, L.S., Zerbes, R.M., Horvath, S.E., Stroud, D.A., von der Malsburg, K., Müller, J.M., Oeljeklaus, S., Perschil, I., Warscheid, B., et al. (2012). Role of mitochondrial inner membrane organizing system in protein biogenesis of the mitochondrial outer membrane. Mol. Biol. Cell *23*, 3948–3956.
18. Körner, C., Barrera, M., Dukanovic, J., Eydt, K., Harner, M., Rabl, R., Vogel, F., Rapaport, D., Neupert, W., and Reichert, A.S. (2012). The C-terminal domain of Fcj1 is required for formation of crista junctions and interacts with the TOB/SAM complex in mitochondria. Mol. Biol. Cell *23*, 2143–2155.
19. Zerbes, R.M., Bohnert, M., Stroud, D.A., von der Malsburg, K., Kram, A., Oeljeklaus, S., Warscheid, B., Becker, T., Wiedemann, N., Veenhuis, M., et al. (2012). Role of MINOS in mitochondrial membrane architecture: cristae morphology and outer membrane interactions differentially depend on mitofilin domains. J. Mol. Biol. *422*, 183–191.
20. Stojanovski, D., Bragoszewski, P., and Chacinska, A. (2012). The MIA pathway: a tight bond between protein transport and oxidative folding in mitochondria. Biochim. Biophys. Acta *1823*, 1142–1150.
21. Mordas, A., and Tokatlidis, K. (2015). The MIA pathway: a key regulator of mitochondrial oxidative protein folding and biogenesis. Acc. Chem. Res. *48*, 2191–2199.
22. Banci, L., Bertini, I., Cefaro, C., Ciofi-Baffoni, S., Gallo, A., Martinelli, M., Sideris, D.P., Katrakili, N., and Tokatlidis, K. (2009). MIA40 is an oxidoreductase that catalyzes oxidative protein folding in mitochondria. Nat. Struct. Mol. Biol. *16*, 198–206.
23. Lynch, M., Field, M.C., Goodson, H.V., Malik, H.S., Pereira-Leal, J.B., Roos, D.S., Turkewitz, A.P., and Sazer, S. (2014). Evolutionary cell biology: two origins, one objective. Proc. Natl. Acad. Sci. USA *111*, 16990–16994.
24. Hampl, V., Hug, L., Leigh, J.W., Dacks, J.B., Lang, B.F., Simpson, A.G., and Roger, A.J. (2009). Phylogenomic analyses support the monophyly of Excavata and resolve relationships among eukaryotic "supergroups". Proc. Natl. Acad. Sci. USA *106*, 3859–3864.
25. Zíková, A., Verner, Z., Nenarokova, A., Michels, P.A.M., and Lukeš, J. (2017). A paradigm shift: The mitoproteomes of procyclic and bloodstream *Trypanosoma brucei* are comparably complex. PLoS Pathog. *13*, e1006679.
26. Ebenezer, T.E., Carrington, M., Lebert, M., Kelly, S., and Field, M.C. (2017). *Euglena gracilis* genome and transcriptome: organelles, nuclear genome assembly strategies and initial features. In Euglena: Biochemistry, Cell and Molecular Biology, S. Schwartzbach, and S. Shigeoka, eds. (Cham: Springer), pp. 125–140.
27. Jackson, A.P., Quail, M.A., and Berriman, M. (2008). Insights into the genome sequence of a free-living Kinetoplastid: *Bodo saltans* (Kinetoplastida: Euglenozoa). BMC Genomics *9*, 594.
28. Pfanner, N., van der Laan, M., Amati, P., Capaldi, R.A., Caudy, A.A., Chacinska, A., Darshi, M., Deckers, M., Hoppins, S., Icho, T., et al. (2014). Uniform nomenclature for the mitochondrial contact site and cristae organizing system. J. Cell Biol. *204*, 1083–1086.
29. Urbaniak, M.D., Guther, M.L., and Ferguson, M.A. (2012). Comparative SILAC proteomic analysis of *Trypanosoma brucei* bloodstream and procyclic lifecycle stages. PLoS ONE *7*, e36619.
30. Butter, F., Bucerius, F., Michel, M., Čičová, Z., Mann, M., and Janzen, C.J. (2013). Comparative proteomics of two life cycle stages of stable isotope-labeled *Trypanosoma brucei* reveals novel components of the parasite's host adaptation machinery. Mol. Cell. Proteomics *12*, 172–179.
31. Peikert, C.D., Mani, J., Morgenstern, M., Käser, S., Knapp, B., Wenger, C., Harsman, A., Oeljeklaus, S., Schneider, A., and Warscheid, B. (2017). Charting organellar importomes by quantitative mass spectrometry. Nat. Commun. *8*, 15272.
32. Mach, J., Poliak, P., Matusková, A., Zárský, V., Janata, J., Lukeš, J., and Tachezy, J. (2013). An advanced system of the mitochondrial processing peptidase and core protein family in *Trypanosoma brucei* and multiple origins of the core I subunit in eukaryotes. Genome Biol. Evol. *5*, 860–875.
33. Hessenberger, M., Zerbes, R.M., Rampelt, H., Kunz, S., Xavier, A.H., Purfürst, B., Lilie, H., Pfanner, N., van der Laan, M., and Daumke, O. (2017). Regulated membrane remodeling by Mic60 controls formation of mitochondrial crista junctions. Nat. Commun. *8*, 15258.
34. Söding, J., Biegert, A., and Lupas, A.N. (2005). The HHpred interactive server for protein homology detection and structure prediction. Nucleic Acids Res. *33*, W244–W248.
35. Pusnik, M., Small, I., Read, L.K., Fabbro, T., and Schneider, A. (2007). Pentatricopeptide repeat proteins in *Trypanosoma brucei* function in mitochondrial ribosomes. Mol. Cell. Biol. *27*, 6876–6888.
36. Panigrahi, A.K., Zíková, A., Dalley, R.A., Acestor, N., Ogata, Y., Anupama, A., Myler, P.J., and Stuart, K.D. (2008). Mitochondrial complexes in

Trypanosoma brucei: a novel complex and a unique oxidoreductase complex. Mol. Cell. Proteomics *7*, 534–545.

37. Týc, J., Faktorová, D., Kriegová, E., Jirků, M., Vávrová, Z., Maslov, D.A., and Lukeš, J. (2010). Probing for primary functions of prohibitin in *Trypanosoma brucei*. Int. J. Parasitol. *40*, 73–83.
38. Mayhew, T.M., Lucocq, J.M., and Griffiths, G. (2002). Relative labelling index: a novel stereological approach to test for non-random immunogold labelling of organelles and membranes on transmission electron microscopy thin sections. J. Microsc. *205*, 153–164.
39. Friedman, J.R., Mourier, A., Yamada, J., McCaffery, J.M., and Nunnari, J. (2015). MICOS coordinates with respiratory complexes and lipids to establish mitochondrial inner membrane architecture. eLife *4*, e07739.
40. Coustou, V., Biran, M., Breton, M., Guegan, F., Rivière, L., Plazolles, N., Nolan, D., Barrett, M.P., Franconi, J.M., and Bringaud, F. (2008). Glucose-induced remodeling of intermediary and energy metabolism in procyclic *Trypanosoma brucei*. J. Biol. Chem. *283*, 16342–16354.
41. Pusnik, M., Charrière, F., Mäser, P., Waller, R.F., Dagley, M.J., Lithgow, T., and Schneider, A. (2009). The single mitochondrial porin of Trypanosoma brucei is the main metabolite transporter in the outer mitochondrial membrane. Mol. Biol. Evol. *26*, 671–680.
42. Basu, S., Leonard, J.C., Desai, N., Mavridou, D.A., Tang, K.H., Goddard, A.D., Ginger, M.L., Lukeš, J., and Allen, J.W. (2013). Divergence of Erv1-associated mitochondrial import and export pathways in trypanosomes and anaerobic protists. Eukaryot. Cell *12*, 343–355.
43. Haindrich, A.C., Boudová, M., Vancová, M., Diaz, P.P., Horáková, E., and Lukeš, J. (2017). The intermembrane space protein Erv1 of *Trypanosoma brucei* is essential for mitochondrial Fe-S cluster assembly and operates alone. Mol. Biochem. Parasitol. *214*, 47–51.
44. Guarani, V., McNeill, E.M., Paulo, J.A., Huttlin, E.L., Fröhlich, F., Gygi, S.P., Van Vactor, D., and Harper, J.W. (2015). QIL1 is a novel mitochondrial protein required for MICOS complex stability and cristae morphology. eLife *4*, e06265.
45. Zerbes, R.M., Höß, P., Pfanner, N., van der Laan, M., and Bohnert, M. (2016). Distinct roles of Mic12 and Mic27 in the mitochondrial contact site and cristae organizing system. J. Mol. Biol. *428*, 1485–1492.
46. Ott, C., Dorsch, E., Fraunholz, M., Straub, S., and Kozjak-Pavlovic, V. (2015). Detailed analysis of the human mitochondrial contact site complex indicate a hierarchy of subunits. PLoS ONE *10*, e0120213.
47. Chojnacka, M., Gornicka, A., Oeljeklaus, S., Warscheid, B., and Chacinska, A. (2015). Cox17 protein is an auxiliary factor involved in the control of the mitochondrial contact site and cristae organizing system. J. Biol. Chem. *290*, 15304–15312.
48. Harner, M.E., Unger, A.K., Izawa, T., Walther, D.M., Ozbalci, C., Geimer, S., Reggiori, F., Brügger, B., Mann, M., Westermann, B., and Neupert, W. (2014). Aim24 and MICOS modulate respiratory function, tafazzin-related cardiolipin modification and mitochondrial architecture. eLife *3*, e01684.
49. Harner, M.E., Unger, A.K., Geerts, W.J., Mari, M., Izawa, T., Stenger, M., Geimer, S., Reggiori, F., Westermann, B., and Neupert, W. (2016). An evidence based hypothesis on the existence of two pathways of mitochondrial crista formation. eLife *5*, e18853.
50. Muñoz-Gómez, S.A., Slamovits, C.H., Dacks, J.B., and Wideman, J.G. (2015). The evolution of MICOS: Ancestral and derived functions and interactions. Commun. Integr. Biol. *8*, e1094593.
51. Mesecke, N., Terziyska, N., Kozany, C., Baumann, F., Neupert, W., Hell, K., and Herrmann, J.M. (2005). A disulfide relay system in the intermembrane space of mitochondria that mediates protein import. Cell *121*, 1059–1069.
52. Eckers, E., Petrungaro, C., Gross, D., Riemer, J., Hell, K., and Deponte, M. (2013). Divergent molecular evolution of the mitochondrial sulfhydryl:cytochrome C oxidoreductase Erv in opisthokonts and parasitic protists. J. Biol. Chem. *288*, 2676–2688.
53. Mani, J., Desy, S., Niemann, M., Chanfon, A., Oeljeklaus, S., Pusnik, M., Schmidt, O., Gerbeth, C., Meisinger, C., Warscheid, B., and Schneider, A. (2015). Mitochondrial protein import receptors in Kinetoplastids reveal convergent evolution over large phylogenetic distances. Nat. Commun. *6*, 6646.
54. Wenger, C., Oeljeklaus, S., Warscheid, B., Schneider, A., and Harsman, A. (2017). A trypanosomal orthologue of an intermembrane space chaperone has a non-canonical function in biogenesis of the single mitochondrial inner membrane protein translocase. PLoS Pathog. *13*, e1006550.
55. Poon, S.K., Peacock, L., Gibson, W., Gull, K., and Kelly, S. (2012). A modular and optimized single marker system for generating *Trypanosoma brucei* cell lines expressing T7 RNA polymerase and the tetracycline repressor. Open Biol. *2*, 110037.
56. Dean, S., Sunter, J., Wheeler, R.J., Hodkinson, I., Gluenz, E., and Gull, K. (2015). A toolkit enabling efficient, scalable and reproducible gene tagging in trypanosomatids. Open Biol. *5*, 140197.
57. McAllaster, M.R., Sinclair-Davis, A.N., Hilton, N.A., and de Graffenried, C.L. (2016). A unified approach towards *Trypanosoma brucei* functional genomics using Gibson assembly. Mol. Biochem. Parasitol. *210*, 13–21.
58. Merritt, C., and Stuart, K. (2013). Identification of essential and non-essential protein kinases by a fusion PCR method for efficient production of transgenic *Trypanosoma brucei*. Mol. Biochem. Parasitol. *190*, 44–49.
59. Schimanski, B., Nguyen, T.N., and Günzl, A. (2005). Characterization of a multisubunit transcription factor complex essential for spliced-leader RNA gene transcription in *Trypanosoma brucei*. Mol. Cell. Biol. *25*, 7303–7313.
60. Wiśniewski, J.R., Ostasiewicz, P., and Mann, M. (2011). High recovery FASP applied to the proteomic analysis of microdissected formalin fixed paraffin embedded cancer tissues retrieves known colon cancer markers. J. Proteome Res. *10*, 3040–3049.
61. Stejskal, K., Potěšil, D., and Zdráhal, Z. (2013). Suppression of peptide sample losses in autosampler vials. J. Proteome Res. *12*, 3057–3062.
62. Käser, S., Willemin, M., Schnarwiler, F., Schimanski, B., Poveda-Huertes, D., Oeljeklaus, S., Haenni, B., Zuber, B., Warscheid, B., Meisinger, C., and Schneider, A. (2017). Biogenesis of the mitochondrial DNA inheritance machinery in the mitochondrial outer membrane of *Trypanosoma brucei*. PLoS Pathog. *13*, e1006808.
63. Katoh, K., Misawa, K., Kuma, K., and Miyata, T. (2002). MAFFT: a novel method for rapid multiple sequence alignment based on fast Fourier transform. Nucleic Acids Res. *30*, 3059–3066.
64. Stamatakis, A. (2014). RAxML version 8: a tool for phylogenetic analysis and post-analysis of large phylogenies. Bioinformatics *30*, 1312–1313.
65. Ronquist, F., Teslenko, M., van der Mark, P., Ayres, D.L., Darling, A., Höhna, S., Larget, B., Liu, L., Suchard, M.A., and Huelsenbeck, J.P. (2012). MrBayes 3.2: efficient Bayesian phylogenetic inference and model choice across a large model space. Syst. Biol. *61*, 539–542.
66. Biasini, M., Bienert, S., Waterhouse, A., Arnold, K., Studer, G., Schmidt, T., Kiefer, F., Gallo Cassarino, T., Bertoni, M., Bordoli, L., and Schwede, T. (2014). SWISS-MODEL: modelling protein tertiary and quaternary structure using evolutionary information. Nucleic Acids Res. *42*, W252–W258.
67. Krogh, A., Larsson, B., von Heijne, G., and Sonnhammer, E.L. (2001). Predicting transmembrane protein topology with a hidden Markov model: application to complete genomes. J. Mol. Biol. *305*, 567–580.
68. Lupas, A., Van Dyke, M., and Stock, J. (1991). Predicting coiled coils from protein sequences. Science *252*, 1162–1164.

STAR★METHODS

KEY RESOURCES TABLE

REAGENT or RESOURCE	SOURCE	IDENTIFIER
Antibodies		
Mouse anti-V5	ThermoScientific (Life Technologies)	Catalog #: 377500; RRID: AB_2533339
Mouse anti-HA	ThermoScientific (Life Technologies)	Catalog #: 26183; RRID: AB_10978021
Rabbit anti-V5	Sigma Aldrich	Catalog #: V8137; RRID: AB_261889
Rabbit anti-HA	Sigma Aldrich	Catalog #: H6908; RRID: AB_260070
Rabbit anti-TbMic10-1	This study	N/A
Mouse anti-HSP70	[36]	N/A
Rabbit anti-TbERV1	[42]	N/A
Rabbit anti-VDAC	[41]	N/A
Rabbit anti-prohibitin	[37]	N/A
Chemicals, Peptides, and Recombinant Proteins		
Proteinase K, recombinant, PCR Grade	Sigma Aldrich (Roche)	Catalog #: 000000003115879001
Digitonin	Sigma Aldrich	Catalog #: D141
Protein G Dynabeads	ThermoScientific (Life Technologies)	Catalog #: 10004D
Dimethyl pimelimidate dihydrochloride	Sigma Aldrich	Catalog #: D8388
Q5 High-Fidelity DNA Polymerase	New England Biolabs	Catalog #: M0491
Critical Commercial Assays		
Direct-zol RNA MiniPrep w/ Zymo-Spin IIC Columns	Zymo Research (Amplicon)	Catalog #: R2050
Human T Cell Nucleofector Kit, 100 reactions	Lonza	Catalog #: VVPA-1002
Bolt TM 4-12% Bis-Tris Plus Gels	ThermoScientific (LifeTechnologies)	Catalog #: NW04120BOX
Deposited Data		
Trypanosomatid ortholog sequences	See Table S1	N/A
927 immunoprecipitation plus TbMic20 and TbMic60 depletome MS^2 data	PRIDE	ID#: PXD009601
Experimental Models: Cell Lines		
TbMic10-1-V5	This study	N/A
TbMic10-2-V5	This study	N/A
ΔTbMic10-1:TbMic10-2↓	This study	N/A
TbMic10-1-HA	This study	N/A
TbMic10-2-HA:TbMic10-1-V5	This study	N/A
TbMic60-HA:TbMic10-1-V5:TbMic60↓	This study	N/A
TbMic16-HA:TbMic10-1-V5:TbMic16↓	This study	N/A
TbMic17-HA:TbMic10-1-V5:TbMic17↓	This study	N/A
TbMic34-HA:TbMic10-1-V5:TbMic34↓	This study	N/A
TbMic32-HA:TbMic10-1-V5:TbMic32↓	This study	N/A
TbMic20-HA:TbMic10-1-V5:TbMic20↓	This study	N/A
TbMic40-HA:TbMic10-1-V5:TbMic40↓	This study	N/A
TbSAM50-HA:TbMic10-1-V5:TbSAM50↓	This study	N/A
Experimental Models: Organisms/Strains		
SMOXP *T. brucei* cell line	[54]	RRID: SCR_004786
Oligonucleotides		
For oligonucleotides used in this study, see Table S3	N/A	N/A

(*Continued on next page*)

Continued

REAGENT or RESOURCE	SOURCE	IDENTIFIER
Recombinant DNA		
pTrypSon	[55]	N/A
pPOTv4	[38]	N/A
pPOT-V5-HygR	This study	N/A
pPOT-HA-NeoR	This study	N/A
Software and Algorithms		
GraphPad Prism 7	GraphPad	https://www.graphpad.com/
Image Lab	Bio-Rad	http://www.bio-rad.com/en-de/product/image-lab-software?ID=KRE6P5E8Z
Geneious 9.1.7	Biomatters	https://www.geneious.com/

CONTACT FOR REAGENT AND RESOURCE SHARING

Further information and requests for resources and reagents should be directed to and will be fulfilled by the Lead Contact, Hassan Hashimi (hassan@paru.cas.cz)

EXPERIMENTAL MODEL AND SUBJECT DETAILS

The procyclic *T. brucei* (RRID: SCR_004786) 927 strain SmOxP cell line [55] served as the parental cell line for all experiments except those depicted in Figures 3D–3H, which utilized 427 strain 29-13 cell line. *T. brucei* were grown at 27°C and ambient atmosphere in SDM79 medium, which was supplemented with 6 mM glucose, or SDM80, a glucose poor medium [40]. Both media contained heat-inactivated 10% (v/v) fetal bovine serum and 7.5 mg/L hemin. Cells were maintained at exponential growth phase as exemplified by the growth curves in Figures 6B, S2C, and S5A plus described in Method Details.

METHOD DETAILS

Generation of T. brucei transgenic cell lines

The SmOxP cell lines were transformed with gene tagging constructs derived from the pPOTv4 vector [56] modified to contain the V5 (with original hygromycin resistance cassette) and HA epitope tags, the latter also with a neomycin resistance marker. Transformants were selected using the appropriate antibiotic. For generation of long hairpin RNAi cell lines, PCR amplicons derived from a given TbMICOS subunit gene were cloned into the pTrypSon vector by the already described Gibson assembly protocol [57]. Constructs for gene knockout were generated by an established fusion PCR approach [58]. Oligonucleotides used for PCR amplification and destination plasmids are given in Table S3.

For SILAC-IP transgenic cell lines based on *T. brucei* 29-13 were generated. The coding sequences of TbMic10-1, TbMic10-2 and TbMic34 were amplified from genomic DNA and cloned into a derivative of pLEW100 modified to enable tetracycline-inducible expression of C-terminal triple, c-Myc tagged proteins after selection with puromycin. In the case of TbMic20, one allele was tagged *in situ* at the N terminus with a single HA epitope via site directed integration of a PCR product amplified from pPURO-HA-TFIIA-1 [59]. Long primers containing homologous regions of the 5′ UTR (positions - 89 to −1 relative to the start codon) and the ORF (positions +4 to + 94) were designed to provide sequences for homologous recombination. Puromycin was used to select for stable transfectants.

T. brucei growth measurements

Cultures were grown in triplicate in the presence and absence of the tetracycline-class antibiotic doxycycline for RNAi-induction. Cell density was counted using the Beckman Coulter Z2 Cell and Particle Counter every 24 H and subsequently diluted to 2×10^6 cells/ml, maintaining cells in exponential phase of growth.

Mitochondria isolation and sub-fractionation

Subfractionation of mitochondria was performed using an established protocol [35]. A suspension of hypotonically isolated mitochondria in 10 mM $MgCl_2$ were initially sub-fractionated into matrix and membrane parts by 10 cycles of snap freezing in liquid N_2 and thawing at RT. The suspension was then centrifuged for 5 min at 10,000 x g at 4°C. The supernatant was collected as the matrix fraction. Part of the pellet was collected as the membrane fraction while the rest was further processed by resuspension in 0.1 M Na_2CO_3. After a 10 minute incubation on ice, the suspension was centrifuged for 20 min at 100,000 x g at 4°C. The supernatant was removed as the peripheral fraction. Fresh 0.1 M Na_2CO_3 was applied to the pellet for another centrifugation as mentioned before.

The pellet was removed as the integral protein fraction. Proteins were precipitated from all fractions with trichloroacetic acid prior to their resolution by SDS-PAGE.

Digitonin preparation of crude mitochondria and quantitative LC-MS^2 and mitoplasts for proteinase K protection assays were done according to an established protocol [54]. Briefly, to obtain crude mitochondrial fractions, 10^8 *T. brucei* cells were treated with 0.015% digitonin (w/v) on ice for 5 min. Mitochondria were concentrated by centrifugation at 6,800 x g for 3 min at 4°C. This pellet was further treated with 0.2% digitonin for 15 min on ice and centrifuged as before to obtain mitoplasts.

Antibody crosslinking to protein G Dynabeads

Fifteen μg of Dynabeads (Thermo Scientific) were washed twice in PBS with 0.02% (v/v) Tween 20 (PBS-T20) and rotated overnight at 4°C with 100μg of mouse anti-V5 or anti-HA antibodies (Thermo Scientific) in 1 mL PBS-T20. Afterward, the beads were washed twice in 0.1 M Triethanolamine in PBS (PBS TEA). The antibodies were conjugated to beads by rotation in PBS TEA supplemented with 6 mg/ml Dimethyl pimelimidate for 30 min at RT twice. The beads were washed again twice in PBS TEA. The beads were then treated with quenching buffer (25 mM ethanolamine in PBS) at RT for 5 min, washed once in PBS, and incubated twice with 1 M glycine pH 3.0 at RT to remove unbound antibody. The beads were washed three times with PBS-T20 and stored at 4°C in 0.09% NaN_3 until needed. Antibodies used in the study are listed in Key Resources Table.

Immunoprecipitations

Hypotonically isolated frozen mitoplast pellets (0.5 mg) were solubilized in IPP50 (50 mM KCl, 20 mM Tris-HCl pH 7.7, 3 mM $MgCl_2$, 10% glycerol, 0.5 mM DTT, 1 mM phenylmethanesulfonyl fluoride (PMSF), complete EDTA free protease inhibitor cocktail (Rosche)) supplemented with 1% Igepal (v/v) for 20 min on ice. After centrifugation (18 000 X g, 15 min, 4°C) the supernatant was added to 1.5 mg of anti-V5 or anti-HA magnetic beads, previously washed three times in 200μl of IPP50 + 1% Igepal for 5 min at RT. The solubilized mitochondria were rotated with beads for 90 min at 4°C. After removal of the flow through, the beads were washed three times in IPP50 + 1% Igepal. Before elution the beads were transferred into a fresh tube. Elution was done in 0.1 M glycine pH 2.0 for 10 min at 70°C and shaking at 1000 rpm. The eluate was neutralized with 1 M Tris pH 8.0. The eluates were further processed for LC-MS^2 analysis or resolved by SDS-PAGE. IPs were performed in triplicate.

Mass spectrometry

Triplicate eluates of co-IP proteins from the 927 strain and duplicate TbMic20 and TbMic60 depletomes were processed by filter-aided sample preparation (FASP) method [60] with some modifications. The samples were mixed with 8 M UA buffer (8 M urea in 100 mM Tris-HCl, pH 8.5), loaded onto a Microcon device with a molecular weight cut-off of 30 kDa (Merck Millipore) and centrifuged at 7,000 × *g* (subsequent centrifugation steps done at 14,000 × *g*) for 30 min at 20°C. The retained proteins were washed with 200 μL UA buffer. The final protein concentrates trapped in the Microcon device were mixed with 100 μL of UA buffer containing 50 mM iodoacetamide and incubated in the dark for 20 min. After the next centrifugation step, the samples were washed three times with 100 μL UA buffer and three times with 100 μL of 50 mM $NaHCO_3$. Sequencing grade trypsin (Promega) was added onto the filter and the mixture was incubated for 18 h at 37°C (enzyme:protein ratio 1:100). The tryptic peptides were finally eluted by centrifugation followed by two additional elutions with 50 μL of 50mM $NaHCO_3$. After FASP, peptides of co-IP proteins were directly extracted into LC-MS vials by 2.5% formic acid (FA) in 50% acetonitrile (ACN) and 100% ACN with addition of polyethylene glycol (20,000; final concentration 0.001%) [61] and concentrated by SpeedVac (Thermo Fisher Scientific) prior to LC-MS analyses.

Triethylammonium bicarbonate was used instead of $NaHCO_3$ during all FASP steps in case of depletome samples. Duplicate TbMic20 or TbMic60 samples were separately labeled using Tandem Mass Tags (TMT6plex; Thermo Fisher Scientific) using the manufacturer's instructions. Labeling efficiency was checked by LC-MS analyses and database searches using variable TMT-related modifications and was found to be > 96% (portion of the correctly labeled peptide spectrum matches (PSMs) out of all PSMs). Individual samples were mixed in the ratio of 1:1:1:1.

Both pooled samples were offline fractionated using basic pH reverse phase liquid chromatography (mobile phase A: 20 mM Ammonium Hydroxide in water; mobile phase B: 20 mM Ammonium Hydroxide in 80% acetonitrile (ACN); stationary phase: XBridge C18 3.5μm, 150 × 3mm; Waters) using the Ultimate3000 UHPLC+ system (SR-3000, LPG-3400 XRS, WPS-3000 TXRS, TCC-3000 RS, VWD-3400 RS). A 30 minute nonlinear gradient (0 min: 0.5% B, 5 min: 10% B, 30 min: 60% B; 35 min: 80% B – system wash; flow rate 0.5 ml/min) was used to fractionate peptides into 33 fractions (1 fraction/min), which were pooled into 11 fractions (1+11+21, 2+12+22, etc.) that were analyzed on the LC-MS system.

LC-MS^2 analysis of peptides

LC-MS^2 analyses of all peptide mixtures were done using RSLCnano system (SRD-3400, NCS-3500RS CAP, WPS-3000 TPL RS) connected to the Orbitrap Elite hybrid spectrometer (Thermo Fisher Scientific). Prior to LC separation, tryptic digests were online concentrated and desalted using a trapping column (100 μm × 30 mm) filled with 3.5-μm X-Bridge BEH 130 C18 sorbent (Waters). After washing of the trapping column with 0.1% FA, the peptides were eluted (flow 300 nl/min) from the trapping column onto an analytical column (Acclaim Pepmap100 C18, 3 μm particles, 75 μm × 500 mm; Thermo Fisher Scientific) by 100 min nonlinear gradient program (1%–56% of mobile phase B; mobile phase A: 0.1% FA in water; mobile phase B: 0.1% FA in 80% ACN). Equilibration of the trapping column and the column was done prior to sample injection to sample loop. The analytical column outlet was

directly connected to the Digital PicoView 550 (New Objective) ion source sheath gas option a PicoTip emitter SilicaTip (New Objective; FS360-20-15-N-20-C12). ABIRD (Active Background Ion Reduction Device, ESI Source Solutions) was installed.

MS data were acquired in a data-dependent strategy selecting up to top 10 precursors based on precursor abundance in the survey scan (350-2000 m/z). The resolution of the survey scan was 60 000 (400 m/z) with a target value of 1×10^6 ions, one microscan and maximum injection time of 200 ms. HCD MS/MS (32 or 36% relative fragmentation energy used for co-immunoprecipitated or depleted samples, respectively) spectra were acquired with a target value of 50 000 and resolution of 15 000 (400 m/z). The maximum injection time for MS/MS was 500 ms. Dynamic exclusion was enabled for 45 s after one MS/MS spectra acquisition and early expiration was disabled. The isolation window for MS/MS fragmentation was set to 2 or 1.4 m/z (co-IP or depletome samples, respectively).

The analysis of the mass spectrometric RAW data files was carried out using the Proteome Discoverer software (Thermo Fisher Scientific; version 1.4) with in-house Mascot (Matrixscience, London, UK; version 2.6) and Sequest search engine utilization. MS/MS ion searches were done at first against modified cRAP database (based on http://www.thegpm.org/crap/; 111 sequences in total) containing protein contaminants like keratin, trypsin etc. MS/MS spectra assigned by Mascot search engine to any cRAP protein peptide with Mascot ion score > 30 were excluded from the next database searches. Final database searches were done against TriTrypDB protein database (http://tritrypdb.org/common/downloads/release-9.0/TbruceiTREU927/fasta/data/TriTrypDB-9.0_TbruceiTREU927_AnnotatedProteins.fasta; number of proteins 11,567). Mass tolerance for peptides and MS/MS fragments were 10 ppm and 0.05 Da, respectively. Oxidation of methionine, deamidation (N, Q) and acetylation (protein N terminus) as optional modification, carbamidomethylation (C) (plus TMT6plex (K, N-term) modifications in case of TMT6plex labeled samples) as fixed modification and one enzyme miss cleavage were set for all searches. A percolator was used for post-processing of the search results. Raw files from all 11 high pH fractions were searched together. Peptides with q-value < 0.01, rank 1 and with at least 6 amino acids were considered only. Proteins matching the same set of peptides were reported as protein groups. Protein groups/proteins were reported only if they had at least one unique peptide.

Co-IP protein abundance was assessed using protein area calculation in Proteome Discoverer. Protein group reports from all individual samples were combined into a single supergroup (SG) report where each SG is list of proteins reported within a single protein group in at least single sample report.

TMT6plex reporter ion intensities of unique peptides were normalized to get equal reporter intensity sum for each channel.

SILAC proteomics

Protein labeling with light and heavy amino acids in cells either expressing or not expressing the tagged bait proteins and subsequent IPs from lysates of 1:1 mixtures of differentially labeled cells were essentially done as described [62]. TbMic10-1 protein complexes were eluted by boiling the resin for 5 min in 60 mM Tris-HCl, pH 6.8 containing 0.1% SDS. The eluate was flash frozen and stored at −80°C until proteins were reduced, alkylated and digested with trypsin in solution and analyze by LC-MS^2 as described [31]. In contrast, IP proteins using tagged TbMic10-2, TbMic34 and TbMic20 as bait were eluted with SDS-PAGE gel loading buffer without β-mercaptoethanol, separated electrophoretically and finally identified after treatment of gel slices and LC-MS^2 analysis exactly as previously described [62]. IPs were performed in triplicate.

Proteinase K protection assay

Mitoplasts resusupended in SoTE buffer (20 mM Tris-HCl pH 7.5, 0.6 M Sorbitol, 2 mM EDTA) from 5 X 10^8 cells were split into 3 tubes. One hundred μg of proteinase K was added to 2 tubes, with one supplemented with 1% Triton-X (v/v). The third tube was left untreated as a mock control. All samples were incubated on ice for 30 min. Five mM PMSF was then added to each tube to stop the reaction.

Transmission electron microscopy

For ultrastructural studies, cells were centrifuged at 620 X g for 10 min at RT and immediately high-pressure frozen using a Leica EM Pact2 high pressure freezing (HPF) machine in the presence of 20% BSA. Freeze substitution was performed in 2% OsO4 diluted in 100% acetone at −90°C for 96 h. Samples were then warmed to −20°C at a rate 5°C/h. After 24 h, the temperature was increased (3°C/h) to 4°C. At RT, cells were rinsed 3 times for 15 min each in 100% acetone, infiltrated in 25%, 50%, 75% SPI-pon resin (SPI) solutions for 1 h at each step. After overnight incubation at 100°C, the samples were polymerized at 60°C for 48 h. Ultrathin sections were stained with ethanolic uranyl acetate (30 min) and lead citrate (20 min). For electron tomography (ET), both sides of sections were covered by gold nanoparticles (NPs) of 10 nm in diameter (BBI) and carbon coated.

For immunogold labeling, cells were fixed with 4% formaldehyde with 0.1% glutaraldehyde in 0.1 M HEPES for 1 h at RT. After washing, pellets of cells embedded in 10% gelatin were immersed in 2.3 M sucrose for 24 h at 4°C and frozen by plunging into liquid nitrogen. Cryosections were cut using a EM UC6 ultramicrotome equipped with a EM FC6 cryochamber (Leica). Cryosections were picked up with a drop of 1.15 M sucrose /1% methylcellulose. Sections were incubated in blocking solution (2% (w/v) nonfat milk in HEPES with 20 mM glycine) for 1 hr at RT and incubated with rabbit anti-HA antibody (Sigma) diluted 1:40. Sections were washed (6 times, 2 min each) with blocking solution and incubated with protein A conjugated to 5 nm gold NPs (UMC, Utrecht) diluted 1:50 for 1h. Samples were washed in HEPES (6 times, 2 min each) and dH2O, contrasted and embedded in 1.8% methylcellulose/0.3% uranyl acetate.

Samples were observed with a JEOL 1010 transmission electron microscope (TEM) operating at an accelerating voltage 80 kV and equipped with a MegaView III CCD camera (SIS). Electron tomograms were collected at tilt steps of 0.6-0.8° using the JEOL 2100F TEM working at 200 kV, equipped with a high-tilt stage plus a Gatan camera (Orius SC 1000) and controlled with SerialEM automated acquisition software. Tomograms were reconstructed using the IMOD software package or Amira. A 3D median filter was applied on reconstructed stacks. Manual masking of the area of interest was employed to generate 3D surface models.

Bioinformatic analysis

Mic10 sequences from various genomes were aligned using MAFFT using the local pair algorithm [63]. Parts of this initial alignment that were represented by $\geq$ 60% gaps were removed via the GAPTREEZ server (https://www.hiv.lanl.gov/content/sequence/GAPSTREEZE/gap.html). This processed alignment was then used to construct a maximum likelihood tree using RAxML [64] with the LG+G model. The fast-bootstrap algorithm from 1000 replicates was used to estimate the best scoring tree and bootstrap support. Additional branching support was then determined by computing Bayesian posterior probabilities using Mr. Bayes 3.2 [65]. Four independent MCMC chains were run for 3×10^6 generations under the LG+G model and default chain parameters. Topology and posterior probabilities were reconstructed after omitting the first 5×10^5 generations.

Homology models generated in SWISSPROT [66]. Transmembrane domain and coiled coil prediction performed using TMHMM v2.0 [67] and COILS [68] servers, respectively.

QUANTIFICATION AND STATISTICAL ANALYSIS

Analysis of immunogold and RNAi transmission electron microscopy data

Immunogold-labeling data were statistically evaluated as follows: NPs were counted in two compartments from randomly acquired areas of sections: mitochondria (subdivided into the following sub-compartments: inner boundary membrane, cristae and a undefined area) and background. Labeling density (LD) was calculated as the number of gold NPs per area. Random images were analyzed until at least 100 NPs were counted in the HA-epitope containing samples. Chi-square analysis, with the null hypothesis of no difference from random distribution, and RLI index were counted according to Mayhew and colleagues [38]. The null hypothesis was rejected in all examined immunodecorated HA-epitope samples. LD data are summarized in Table S2.

Cristae lengths were measured using ImageJ on images of randomly acquired mitochondrial sections. Between 39 and 74 mitochondrial sections were counted to measure the length of at least 200 cristae. Statistical significance of cristae lengths in comparison to the parental cell line controls were determined by unpaired Student's t test using GraphPad Prism 7 software.

Analysis of TbMic20 and TbMic60 depletome data

TbMic20 and TbMic60 RNAi 4 dpi for depletome analysis, which includes their respective non-induced controls, was performed in duplicate. Proteins with $\log_2$ transformed relative values $\geq$ 1.6-fold in each RNAi relative to non-induced controls were considered to be part of the TbMic20 depletome. For determination of a secondary effect of TbMic20 RNAi on OXPHOS proteins compared to matrix controls, all $\log_2$ relative values of proteins fitting into the catagories as defined by Ziková and colleagues [25] from each duplicate was incorporated into a violin plot. Statistical significance of subunits of each respiratory chain complex compared to core matrix proteins was determined by unpaired Student's t test using GraphPad Prism 7 software.

DATA AND SOFTWARE AVAILABILITY

The mass spectrometry proteomics data pertaining to *T. brucei* 927 IPs plus TbMic20 and TbMic60 depletomes have been deposited to the ProteomeXchange Consortium via the PRIDE partner repository with the dataset identifier PRIDE: PXD009601.